Reliability Engineering and System Safety 273 (2026) 112256

Contents lists available at ScienceDirect

Reliability Engineering and System Safety

journal homepage: www.elsevier.com/locate/ress

Travel time resilience of national multimodal transport systems under extreme events: A passenger-oriented framework

Hui Zhang [a], Min Ouyang [b,c,*], Min Xu [d], Wenjing Sun [b], Liu Hong [b,c], Duantengchuan Li [a]

[a] School of Information Management, Wuhan University, Wuhan, 430074, China
[b] School of Artificial Intelligence and Automation, Huazhong University of Science and Technology, Wuhan, 430074, China
[c] Key Lab. for Image Processing and Intelligent Control, Huazhong University of Science and Technology, Ministry of Education, Wuhan, 430074, China
[d] School of Public Administration, Dongbei University of Finance and Economics, Dalian, Liaoning, 116025, China

ARTICLE INFO

Keywords:
National multimodal transport system
Travel time-based resilience
Extreme events
Passenger-oriented

ABSTRACT

National multimodal transport systems (NMTSs) are vital to intercity mobility and economic development, yet increasingly vulnerable to extreme events. Existing resilience assessments largely focus on single-mode or regional-scale systems and fail to address the resilience of NMTSs, considering their large-scale, multi-modal, timetable-dependent nature. In response to this challenge, the paper proposes a passenger-oriented framework to assess the resilience of NMTSs under extreme events. A dynamic functionality network is constructed, integrating scheduled services, intermodal transfers, and time-dependent travel paths. Based on this network, a resilience model is formulated using daily passenger demand and minimum travel time matrices. Two computational methods, a critical nodes-based method and a segment computation-based method, are designed to ensure computational efficiency. The framework is applied to the coupled road, high-speed rail, and airline system in mainland China under COVID-19 lockdowns and a heavy rainstorm in Zhengzhou. Results show that the daily proportion of affected passengers during city lockdowns ranges from 0.01% to 10.07%, with impacts strongly correlated with city GDP and network size. In the rainstorm case, 6.44% of passengers were affected, with an average delay of 167.12 min. The proposed framework offers a transferable and computationally efficient approach for national-scale resilience assessment and transport planning.

1. Introduction

National transport systems, comprised of highway, railway, airline, and so on, are vital to intercity mobility and national productivity [1–5]. As different transport modes of national transport systems become increasingly interconnected, intermodal transfers and shared demand have become increasingly common [6,7]. In China, for example, the 12,306 air-rail intermodal services now cover over 80 cities, and where formal services are absent, roads provide the critical station–airport connectors that enable passengers' door-to-door travel. Collectively, road, rail, and air carry over 99 % of intercity passengers [8]. This interconnection broadens travel choice and operational flexibility but also creates cross-modal interdependencies [9,10]. These realities motivate national, multimodal, and passenger-oriented approaches for transport planning and investment [11,12].

Given their extensive geographic coverage, national multimodal transport systems (NMTSs) are highly exposed to extreme events, from natural hazards such as floods and typhoons to human-induced disruptions like regional lockdowns [13–15]. These events can damage infrastructure and simultaneously suspend scheduled services (e.g., train and flight cancellations), sharply reducing passenger mobility [16]. For example, the 7.20 Zhengzhou rainstorm in 2021 flooded rail stations and the airport, delaying or canceling more than 1000 trains and over 500 flights in a single day, and reportedly affecting millions of travelers. While intermodal redundancy offers alternative routes during disruptions, cross-modal interdependencies also transmit failures: flooded arterials sever access/egress to rail stations and airports; hub station/airport closures propagate timetable knock-ons and missed transfers [17–19]. These risks are expected to intensify under climate change and rapid urbanization [1,20,21]. Consequently, understanding and enhancing NMTS resilience from the passenger perspective—how extreme events reshape door-to-door travel time and journey reliability—has become a pressing research priority [22].

Despite growing interest in transport system resilience, most

* Corresponding author.
E-mail address: min.ouyang@hust.edu.cn (M. Ouyang).

https://doi.org/10.1016/j.ress.2026.112256
Received 29 April 2025; Received in revised form 15 December 2025; Accepted 18 January 2026
Available online 19 January 2026

national-scale studies focus on single-mode (e.g., railway or highway) or overlook critical factors such as passenger demand, travel time variability, and service schedules [9,23–25]. Multimodal, travel time–based assessments are typically confined to urban or regional contexts, where system complexity is more tractable [19,26–28]. Extending such analyses to NMTSs introduces several modeling and quantification challenges. First, the multimodal and timetable-constrained nature of NMTSs makes it difficult to accurately model passengers' routing behavior and transfer decisions across modes [29,30]. Second, jointly representing physical damage and service-level disruptions to quantify their combined passenger impacts—an integration rarely attempted [31]. Third, the travel time–based resilience problems at the national scale are computationally intensive, especially when accounting for failure uncertainty [32,33]. Most algorithms developed for urban-scale systems are not scalable to national networks involving hundreds of thousands of components and detailed timetable data [34,35]. Collectively, the large-scale, multimodal, and timetable-dependent characteristics of NMTSs, combined with the diversity and uncertainty of extreme events, make travel time–based resilience both methodologically and computationally.

In response, this study proposes a passenger-oriented framework for assessing the travel time resilience of NMTSs under extreme events. The framework ingests multimodal transport data (road, rail, and air), OD demand, and day-by-day event calendars; and outputs time-dependent OD travel times, daily functionality metrics, and cumulative resilience loss. It offers several key contributions. First, it addresses the modeling complexity by constructing a dynamic functionality network of NMTSs and formulating a resilience model that integrates multimodal routing, timetable constraints, diverse disruption scenarios, and travel demand of passengers. Second, to cope with the huge computational challenge, two solution methods are proposed to efficiently calculate the travel time resilience under different application scenarios. Third, the methodology is applied to the resilience assessment of the coupled road, high-speed railway (HSR), and airline system in mainland China under two real-world events—COVID-19 city lockdowns, representing operational service disruptions, and a heavy rainstorm in Zhengzhou, representing infrastructure damage. This study serves three audiences: passengers by predicting door-to-door times and enabling disruption-aware rerouting; operators by estimating achievable itineraries under current timetables and testing staged recovery policies; and planners by identifying key correlates of resilience outcomes and intermodal bottlenecks. The rest of this paper is organized as follows. Section 2 reviews recent literature on national transport system resilience. Section 3 describes the detailed methodology of this paper. Section 4 presents a case study on the coupled road, HSR, and airline system in mainland China. Section 5 provides conclusions and directions for future research.

2. Literature review

Many disaster-related concepts have been utilized to study the performance of transport systems against disruptions, including reliability, risk, vulnerability, robustness, flexibility, survivability, and resilience. Among them, reliability is defined as the probability that a network remains operative given the occurrence of a disaster or disruptive event [36,37]; risk is used to characterize the threat of a disaster event in terms of its likelihood of occurrence and consequence, and typically measured as the probability of an event arising and its corresponding effects [38]; vulnerability is usually quantified as the functionality drop under a disruptive event [39], and robustness can be regarded as the opposite of vulnerability [36]; flexibility captures the inherent capacity of a system to cope with uncertainty [40]; survivability is the ability to withstand sudden disturbances to transport functionality while meeting original demand [41]. This study mainly focuses on resilience, which measures the capability of a system to withstand internal/external disruptions and rapidly recover from them [42–44]. Compared with other terms, resilience offers a much broader framework to cope with disruptions including preparedness, response, recovery, and adaptation [17,45], and resilient transport system is thus regarded as an efficient means to cope with the challenges imposed by lifeline interdependencies, multiple evolving hazards, and climate change.

2.1. Resilience of single-mode national transport systems

National-scale quantitative resilience studies for individual transport modes—especially rail and air—fall into three streams. One stream could be characterized as topology-based resilience analysis, where complex-network metrics, such as network efficiency [46,47], connectivity [37,48], or largest component size [49,50], are used to measure system functionality. For example, Xiao et al. [37] identified critical HSR stations and trains via their impacts on network connectivity, and Fan et al. [51] proposed a degree-deviation flight-addition strategy that improves the robustness of European air networks under random and centrality-based attacks. The second stream proposed flow-based metrics to capture service disruptions, including the number of canceled/delayed trains (or flights) [52–55] and the service frequency [56]. Janić [57], for example, provides a data-driven resilience assessment of FedEx Express during the 2010 "Snoverkill" blizzard based on real data on canceled flights, and similar approaches have been applied to the U. K. rail system [58].

The third stream uses travel-time outcomes as resilience indicators. Common functionality metrics include average travel time [59–61], travel delay [62–65], weighted travel time [66,67], delayed passenger flow [68], and accessibility [69,70]. Xue et al. [64] quantify how severe rainfall perturbs HSR travel times across different spatial-temporal scenarios, while Tang et al. [71] design a three-stage HSR recovery—rescue/additional trains, in-area timetable optimization, and external coordination—to minimize passenger delays in the Greater Bay Area. Together, these studies underscore the central role of timetables and travel-time modeling in assessing post-disaster transport functionality [71–73].

2.2. Resilience of national multimodal transport systems

Despite growing intermodal coupling, rigorous national-scale multimodal resilience studies remain scarce and mostly focus on paired systems, especially rail-air [74,75]. Fang et al. [53] propose a multi-stage resilience framework for typhoon impacts assessment and show that rail-air complementarity can enhance system resilience. Using the train/flight flow-based metrics, Chen and Wang [52] estimated the impacts of severe weather events on HSR and airline in China. Utilizing the travel time-based metrics, Zhang et al. [4] analyzed the coupled rail and air system against localized events. Studies on road-rail coupling systems also appear: Chen et al. [59] evaluated pluvial-flood impacts using topology-based travel time delay and found the coupled road-HSR network more resilient than single-mode counterparts; Misra and Padgett [76] assessed the resilience of a national rail-highway freight system under earthquakes using freight volume and cost as functionality metrics.

Yet in many countries, road, rail, and air jointly deliver nearly all intercity mobility (e.g., >99 % in China), and only a few studies integrate all three modes for resilience analysis. Chen and Lu [77] construct a topology-based resilience model for the Greater Bay Area road–rail–air system under random failures, targeted attacks, and natural hazards, proposing a node-importance recovery policy; Stamos et al. [78] analyze a three-city air-rail-road network under extreme weather using a data-driven method. These tri-modal studies remain topology-centric and do not incorporate timetables.

Crucially, tri-modal coupling is realized through passengers' door-to-door chains—shared demand and intermodal transfers in normal operations—and through cross-modal substitution and cascade pathways under disruption (e.g., flight cancellations shifting to rail or road). Omitting any mode therefore biases delay, accessibility, and affected-

passenger estimates and obscures recovery levers. This motivates a national-scale, passenger-oriented, timetable-aware framework that represents all three modes jointly.

3. Methodology

This study develops a passenger-oriented framework to quantify the impact of extreme events on national multimodal transport systems (NMTSs), with an explicit focus on travel time and travel flow (Fig. 1). The framework comprises six modules:

(1). Multi-source data integration: Assemble transport system data (e.g., railway layout, train and flight timetables, road network), OD demand data, extreme-event data, and socio-economic data.
(2). Functionality network modeling: Construct a unified, dynamic functionality network G with three modal layers (road, rail, air) coupled by transfer links, that supports time-dependent routing and travel time calculation.
(3). Extreme-event modeling. Map daily physical damage and service suspensions to network G via a damage state vector X_d; produce the disrupted network $G(X_d)$ for each day of the event.
(4). Functionality loss calculation. Compute OD travel times on $G(X_d)$ using a time-dependent minimum travel-time algorithm (MTTA); combine with OD demand to obtain daily functionality loss A_d.
(5). Resilience assessment. Aggregate A_d over the event window to derive resilience loss RL; accelerate national-scale assessment by proposing two efficient methods.
(6). Output. The framework outputs time-dependent OD travel times, daily functionality, and multi-scale resilience loss, which inform disaster response and resilience planning.

The data sources and output are described in Section 4 (Case study). The remainder of this section details the other four modules.

3.1. Functionality network modeling of NMTSs

Although road, rail, and air systems are physically independent and operate under distinct rules, they jointly serve door-to-door journeys and share a common "travel time" attribute from the passenger's perspective. This section therefore integrates the three subsystems into a unified functionality network capable of capturing end-to-end passenger behaviors. Passenger movements are classified into four categories—-road travel, rail travel, air travel, and inter-mode transfers—leading to a three-layer network structure (road, rail, and air) interconnected by directed transfer links (Fig. 2).

(1). Road layer

The road layer is modeled as an undirected weighted network $G^R = (N^R, E^R, W^R)$, where N^R is the set of road intersections, E^R is the set of road segments, and W^R record travel time along each edge. The travel time along a link is determined by segment length, speed limit, and disruption status (e.g., closures or capacity reductions). The nationwide road layer in this study includes both intercity expressways (connecting cities) and urban roads (primarily enabling within-city access/egress to stations/airports and supporting intra-city inter-terminal transfers).

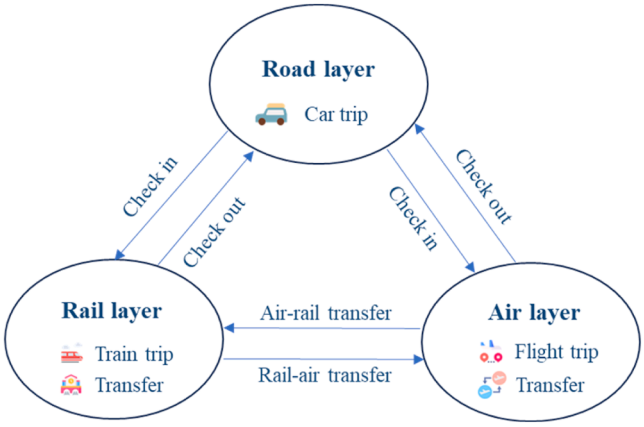

Fig. 2. The three layers of the NMTSs and the passenger trips in each layer.

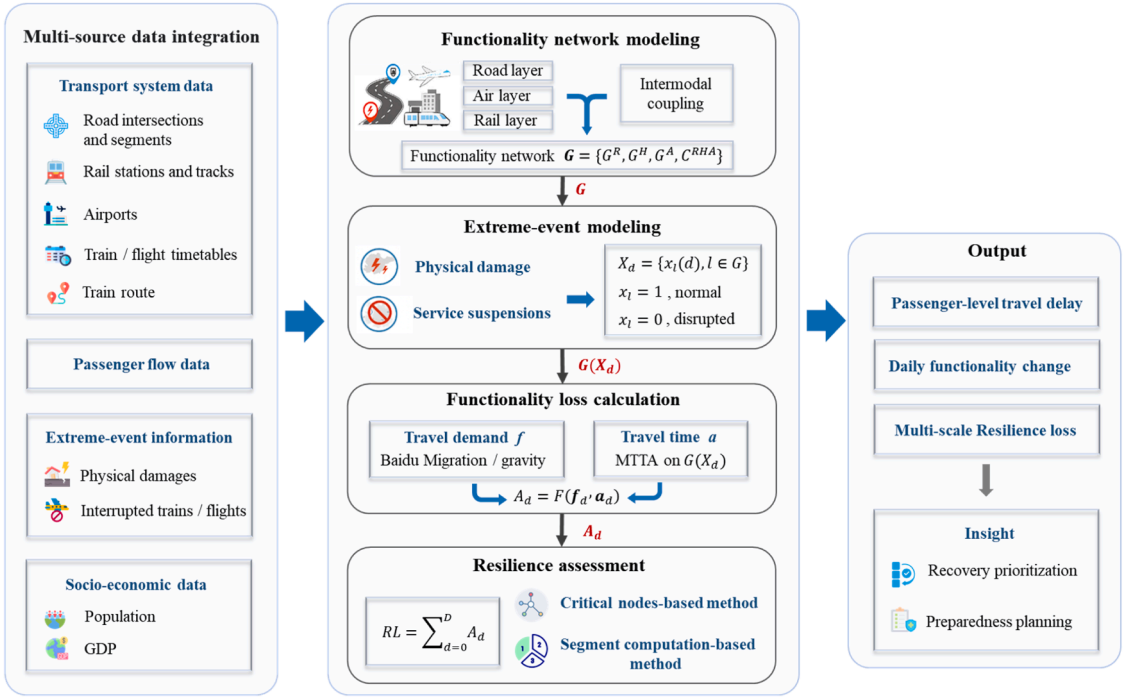

Fig. 1. The demonstration of the passenger-oriented resilience assessment framework for NMTSs.

(2). Rail layer

Rail travel comprises inter-station train trips and identical-mode transfers within a station. To explicitly capture passenger waiting and platform changes, each station n is modeled as two nodes, i.e., a departure node n_{dp} and an arrival node n_{ar}, representing the departure platform and arrival platform, respectively. A train trip from station i to station j on train h is modeled as a timetable-related link from i_{dp} to j_{ar}. An identical-mode transfer within station n is modeled as a transfer link from n_{ar} to n_{dp} (Fig. 3a-b).

The weight of each link corresponds to its travel time. For a timetable-related link l from i_{dp} to j_{ar} via train h, its travel time consists of two parts. The first part is the running time of train h, quantified as the scheduled arrival time at_l at station j minus its scheduled departure time dt_l at station i. The second part is the waiting time for train h, which depends on the passenger's arrival time at the departure platform i (t_i). If one arrives at the departure station before the train departs, the travel time equals the scheduled arrival time minus the passenger's arrival time; otherwise, the passenger waits until the next scheduled service, as shown in Fig. 3c and Eq. (1). Identical-mode transfer links are assigned the minimum platform transfer time (MPTT) for the respective station. This transfer time represents the minimum time required for passengers to move between platforms and board a subsequent train. Notably, trains themselves do not traverse transfer links; these links solely characterize passenger transfers.

$$w_l = \begin{cases} at_l - t_i, & t_i \le dt_l \\ 1440 + at_l - tm_i, & t_i > dt_l \end{cases} \quad (1)$$

The rail layer is thus modeled as $G^H = \left(N^H_{dp}, N^H_{ar}, L^H, L^{HH}, W^H, W^{HH}\right)$. N^H_{dp} and N^H_{ar} denote the set of departure nodes and arrival nodes of all stations, respectively; L^H is the timetable-related link set with time-dependent weight W^H; L^{HH} records the identical mode-based transfer link set with transfer times W^{HH} determined by station design.

(3). Air layer

The air layer mirrors the rail construction: $G^A = \left(N^A_{dp}, N^A_{ar}, L^A, L^{AA}, W^A, W^{AA}\right)$. N^A_{dp} and N^A_{ar} denote the set of departure nodes and arrival nodes of all airports, respectively; L^A is the airline timetable-related link set with a weight set W^A; L^{AA} records the identical mode-based transfer links set inside all airports, and W^{AA} records the corresponding transfer time.

(4). Intermodal coupling

Three families of transfer links couple the layers: For the transfer between road and rail layers, check-in links $L^{R\to H}$ connect the nearest road node of each rail station to its departure node. And check-out links $L^{H\to R}$ connect the arrival node of each rail station to its nearest road node. Their weights $W^{R\to H}$ and $W^{H\to R}$ include access/egress walking and fixed penalties for ticketing/security where applicable. Analogously, check-in/out links $L^{R\to A}/L^{A\to R}$ with weights $W^{R\to A}/W^{A\to R}$ represent the transfer between road and air layers. For co-located multimodal hub facilities (e.g., an airport with an integrated rail station), directed intermodal links $L^{H\to A}/L^{A\to H}$ with fixed transfer times $W^{H\to A}/W^{A\to H}$ covering check-in/out, security, and baggage are built. Such air–rail integration is common in practice; in China, for example, the 12,306 air–rail program currently serves 46 cities. Where no direct facility exists, rail–air transfers can be realized via the urban roads (rail→road→air). Then, C^{RHA} is defined to record all these transfer links and their weights.

Finally, the NMTS is modeled as a weighted directed network $G = \{G^R, G^H, G^A, C^{RHA}\}$. For transparency and reproducibility, Appendix A provides a worked example that enumerates all links and their weights, and traces a sample passenger itinerary to illustrate how actual arrival times propagate. Unlike many static multi-modal networks that overlook the timetables of trains and flights [59,76], our modeling method introduces a dynamic functionality network G that incorporates time-varying weights for timetable-related links. In this way, the travel time of a specific OD pair varies depending on the departure time. This time-dependent variation is a key characteristic of the functionality network when assessing travel time-based resilience. Furthermore, the above network modeling method is also applicable to other subsystems of NMTSs, such as the coupled road and railway system, the coupled road and airline system, and each individual system.

3.2. Modeling of extreme events

The impacts of extreme events on transport systems can generally be classified into two categories. The first type involves direct physical damage to transport infrastructure. For example, the 7.20 Zhengzhou rainstorm inundated road segments, rail stations, and tracks. The second

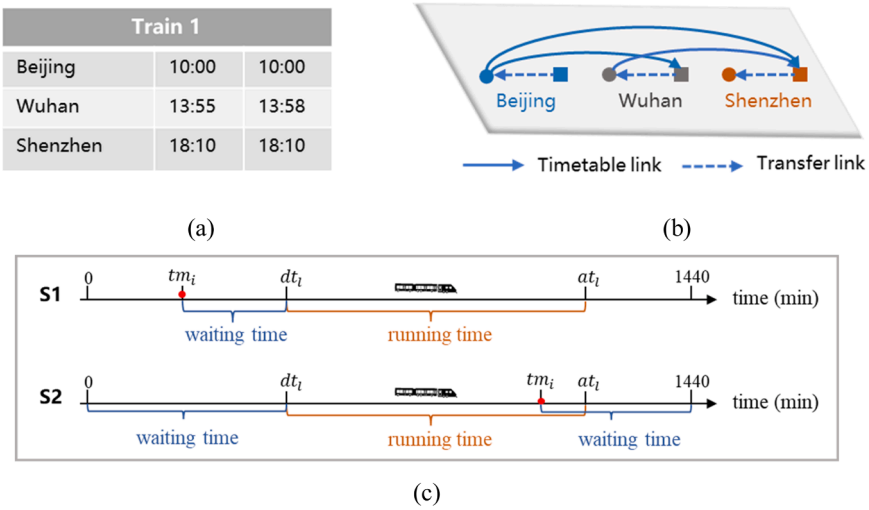

Fig. 3. (a) The timetable of train 1. (b) the network model of train 1 and the three stations, where each train travel is modeled by a timetable-related link from the departure node (dots) of the departure station to the arrival node (squares) of the arrival station. (c) two situations recording the waiting time and in-train time along a timetable-related link.

type comprises service-level disruptions without physical damage. A prominent case is the COVID-19 outbreak, during which the lockdown of Wuhan (January 23 to April 8, 2020) led to a large-scale suspension of road, rail, and air services. Both types of impacts can be consistently represented by modeling their effects on the operational status of nodes and edges in functionality network G. Specifically, for each day d, the impact of an extreme event on the transport system is captured by a damage state vector X_t in Eq. (2). x_l is a binary variable indicating the operational state of component l (1 for functional state, 0 for damaged state. This component–time formulation naturally accommodates phased or asynchronous failure and recovery across modes and assets (different components may fail or resume on different days).

$$X_d = \{x_l(d),\ l \in G\} \tag{2}$$

At the implementation level, the framework systematically collects daily disruption information during each extreme event, encompassing both physical damage (e.g., inundated stations, collapsed roads) and service disruptions (e.g., road closures, train suspensions, flight cancellations). It is assumed that if any station or track along a train's route experiences physical damage, the corresponding train service is canceled. Subsequently, these disruptions are mapped onto the functionality network G by establishing the correspondence between disrupted components (physical infrastructure or scheduled services) and their network representations. Specifically, each component l in G corresponds to a set of underlying physical elements and scheduled trains/flights, denoted as Z^l. Component l is considered disrupted if any element in its corresponding set fails, as shown in Eq. (3). For instance, the state of a timetable-related link from station i to station j via train h depends on the states of station i, station j, and train h.

$$x_l(d) = \prod_{i \in Z^l} x_i(d),\ l \in G \tag{3}$$

This formulation enables both physical damages and service suspensions to be consistently encoded into the damage state vector, thereby providing a unified representation of multimodal disruptions under extreme events.

3.3. Functionality loss calculation

The previous subsection modeled how extreme events affect the damage state of network G, and produce a disrupted network $G(X_d)$ each day. This subsection translates those impacts into passenger-level consequences and calculates the day-to-day system functionality loss. When disruptions occur, certain trips may become infeasible—either direct trips whose origin or destination lies within the affected region, or transit-dependent trips whose pre-event itineraries traverse nodes/links in that region. Travelers may wait for services to resume or adapt by re-routing and/or changing modes. To reflect these effects, the functionality loss on day d, A_d is evaluated from passenger travel performance using an OD demand matrix $\boldsymbol{f}_d = \left\{f_{ij}(d),\ i, j \in N^Z\right\}$ and a corresponding OD travel-time matrix $\boldsymbol{a}_d = \left\{a_{ij}(d),\ i, j \in N^Z\right\}$ on day d, as shown in Eq. (4), where N^Z records the set of origins and destinations.

$$A_d = F(f_d, a_d) \tag{4}$$

This formulation is flexible: by choosing $F(\cdot)$, one can report average delay, the proportion of delayed passengers, or accessibility indices [79–81].

Ideally, $\boldsymbol{f}$ should capture temporally resolved passenger flows (e.g., hourly or minutely), and the route choice decisions should be mediated by many complex factors including travel time, travel cost, transfer times, and mode preferences (Appendix A.4). However, such granular data are rarely available at the national scale. As a practical simplification, and in line with prior transport accessibility and resilience studies [80,82–84], this study assumes that each passenger selects the daily fastest travel path. This implies that all passengers on day d are represented by the itinerary achieving the daily minimum travel time across all feasible multimodal paths and departure times (Appendix A.4). This provides the lowest bound estimation of travel time, and implicitly captures the adaptive re-routing behavior under disruption. Under this assumption, f_{ij} represents the daily aggregated travel demand from zone i to zone j, which can be sourced from empirical datasets (e.g., Baidu Migration) or standard demand models (e.g., gravity). The OD travel time a_{ij} denotes the daily minimum travel time from zone i to zone j across all feasible multimodal paths and departure times on the disrupted network G, as shown in Eq. (5). Where DT denotes the set of departure time that ranges from 0:00 am to 24:00 pm with a time interval of 10 min, and $c_{ij}(t)$ is the minimum travel cost (in-vehicle time + time-dependent waiting + transfer times) at departure time t.

$$a_{ij}(d) = \min_{t \in DT} c_{ij}(t),\ \forall i, j \in N^Z \tag{5}$$

To compute $c_{ij}(t)$, the standard static Dijkstra algorithm is inapplicable since timetable-related links in network G have time-varying weights [85]. This section therefore proposes a Minimum Travel-Time Algorithm (MTTA) for time-dependent networks. MTTA computes the minimum travel times $c_{mn}(t_m)$ from a given origin m and departure time t_m over network G as follows:

Step 1. Set travel time $c_{mm}(t_m) = 0$, and $c_{mn}(t_m) = bigM$ for all $n \neq m$. Define a vector $\{\Omega_m(n)\}$ to record the current travel time from m to n, with all elements initially set as $bigM$ (a sufficiently large number); note that $\Omega_m(m)$ is not included in $\{\Omega_m(n)\}$.
Step 2. Define n^* to record the current traversing node, and set n^* as m.
Step 3. Identify all links l directly connected to n^* (i.e., $o(l) = n^*$, $o(l)$ and $d(l)$ separately denote the origin and destination node of link l), calculate the travel time along link l when departing at t_{n^*}, i.e., $\tau_l(t_{n^*})$. It equals the link weight or $bigM$, depending on whether link l is disrupted, as shown in Eq. (6).

$$\tau_l(t_{n^*}) = x_l w_l(t_{n^*}) + (1 - x_l) bigM,\ \forall o(l) = n^* \tag{6}$$

where $w_l(t_{n^*})$ is a constant weight value for those constant links, including road edges, identical-mode transfer links, check-in and check-out links. Whereas its value varies with the passenger's arrival time t_{n^*} for timetable-related links, as expressed in Eq. (1).

Step 4. Update $\Omega_m(d(l)) = c_{mn^*}(t_m) + \tau_l(t_{n^*})$. Identify the minimum value in $\{\Omega_m(n)\}$, record the corresponding node as n^*, set $c_{mn^*}(t_m) = \Omega_m(n^*)$, $t_{n^*} = t_m + c_{mn^*}(t_m)$, and remove $\Omega_m(n^*)$ from $\{\Omega_m(n)\}$.
Step 5. Repeat steps 3–4 until $\{\Omega_m(n)\}$ is empty or all elements in $\{\Omega_m(n)\}$ equal $bigM$.

By running MTTA over all departure times $t \in DT$ for each OD pair, the OD travel time $a_{ij}(d)$ is obtained as Eq. (5). Coupling these times with OD demands $f_{ij}(d)$, the daily system functionality loss A_d can be calculated. For better clarity, Appendix A provides a worked example that illustrates how passenger routes and travel times change after a disruption event.

3.4. Travel time resilience assessment

This section evaluates the travel time-based resilience for NMTSs. Here, the resilience loss RL is the integral of the daily functionality loss A_d over the entire event influencing period $[0, D]$ [86]:

$$RL = \sum_{d=0}^{D} A_d \tag{7}$$

A direct evaluation of RL would repeat MTTA (Section 3.3) for all OD pairs $(i, i) \in N^Z \times N^Z$, for all departure time $t \in DT$, and across all days $d \in [0, D]$. However, this simple repetition-based method (SRM) is computationally expensive for NMTSs with large road networks (e.g., for mainland China, a single OD MTTA can take days, implying decade-level wall-clock time for full SRM). To address this, two efficient methods—the critical-nodes method (CNM) and the segment-computation method (SCM)—that yield exact travel-time while reducing runtime by orders of magnitude.

(1). Critical nodes-based method

Given that resilience is typically evaluated on a limited set of representative nodes—one per analysis zone [87,88], the critical nodes-based method (CNM) replaces the full road network with a compact critical road network among nodes that actually mediate multimodal journeys. Two types of critical road nodes are used: (i) intermodal access nodes N^I (count k^I; red dots in Fig. 4a), defined as the road nodes nearest to rail stations and airports, which connect the road layer to the rail and air layers. (ii) OD representative nodes N^Z (count k^Z; red stars in Fig. 4a), whose door-to-door travel times underpin the functionality calculation in Eq. (4). Notably, OD nodes are task-driven but chosen by deterministic, ex-ante rules to remove arbitrariness. Typical national-scale tasks include: (a) intercity travel time analysis, where each city's central road node is taken as the OD node; (b) key-facility accessibility, where all road nodes serve as origins and the road nodes nearest to each facility serve as destinations; and (c) station/airport accessibility, where all HSR stations and airports are taken as OD nodes.

Operationally, the CNM first extracts a fully connected critical road network $G^C = (N^C, E^C, W^C)$, where $N^C = N^I \cup N^Z$ denotes the critical node set. Any two critical nodes are connected by an undirected link in E^C; with link weight in W^C equals to the fastest travel time between two endpoints on the full road network under X_d. Next, this critical network is integrated with the rail and air layers to form a hybrid network $G^{CHA} = \{G^C, G^H, G^A, C^{RHA}\}$ (Fig. 4b), and the MTTA is executed on this reduced network to compute minimum travel times and derive resilience loss. It should be noted that the computational cost of CNM is governed by k^Z, with its computational time complexity as $O\left(k^{Z^2}\right)$ (Fig. 5). Consequently, CNM is highly efficient when $k^C \ll k^R$ but its advantage diminishes as k^C approaches the size of the original road network.

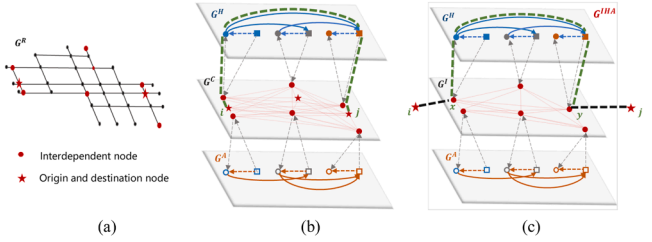

Fig. 4. The simplified versions of network G. (a) the original road network with red nodes for intermodal access nodes and red stars for OD representative nodes. (b) the simplified network G^{CHA}, where the light pink lines denote links in E^C; the green dashed lines indicate the travel path from origin i to destination j via G^{CHA}. (c) The simplified network G^{IHA}, where the light pink lines denote links in E^I; the travel path from origin i to destination j consists of three parts: road-based travel from i to x, G^{IHA}-based travel from x to y, and road-based travel from y to j.

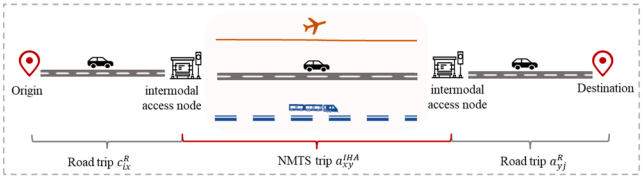

Fig. 5. The three segments of the travel from origin i to destination j. the access/egress road legs may be purely urban (same-city terminal) or a mix of urban roads and expressways when using a nearby city's terminal.

(2). Segment computation-based method

In response to the huge computational time of CNM when $k^C \approx k^R$, the segment computation-based method (SCM) is further proposed. In this method, a trip from origin i to destination j is decomposed into three segments: a road travel from i to x, a NMTS travel from x to y, and a road travel from y to j, where $x, y \in N^I$ are intermodal access nodes (Fig. 5). Among these, only the middle segment is multimodal and computationally expensive. To accelerate evaluation, the method precomputes and stores the NMTS travel times between all intermodal access node pairs as a time-dependent lookup table. The OD earliest-arrival at departure time t is then obtained by min-plus composition of two road legs with a single trunk lookup (evaluated over candidate station pairs), as shown in Eq. (8). c_{ix}^R and c_{yj}^R denote the road-only travel time from i to x and from y to j, respectively. $c_{xy}^{IHA}\left(t + c_{ix}^R\right)$ the precomputed multimodal time from x to y at time $t + c_{ix}^R$.

$$c_{ij}(t) = \min_{x,y \in N^I} \left\{ c_{ix}^R + c_{xy}^{IHA}\left(t + c_{ix}^R\right) + c_{yj}^R \right\}, \; i, j \in N^Z, t \in DT \tag{8}$$

Operationally, SCM first extracts a road graph among intermodal access nodes $G^I = (N^I, E^I, W^I)$, E^I connects access-node pairs and W^I records the fastest road travel time between the two endpoints of each link under X_d. Next, it builds a simplified multimodal network $G^{IHA} = \{G^I, G^H, G^A, C^{RHA}\}$, and runs MTTA to precompute $c_{xy}^{IHA}(t)$ for all $x, y \in N^I$ and $t \in DT$ via G^{IHA}. Finally, OD queries are realized using Eq. (8) with two road computations and one table lookup, avoiding repeated multimodal searches. Because the cost of SCM scales primarily with the number of access nodes k^I—which is typically much smaller than k^R—SCM is particularly advantageous when k^Z is large (e.g., many or all nodes are OD). The resulting OD times feed into the daily functionality and resilience aggregation as described above.

In implementation, given the multimodal network G, its day-by-day damage states X_d, and the OD set N^Z used in the functionality metric, the evaluation method is selected based on k^Z. When k^Z is small (e.g., for a single OD pair), the CNM is adopted, which contracts the road layer to a compact graph on critical nodes and thereby avoids repeated searches over the full road mesh. When k^Z is large (e.g., many or all nodes are OD), the SCM is selected, which precomputes a lookup table of multimodal station-to-station times, thereby eliminating redundant multimodal searches. The threshold for method selection k^{Z*} is case-dependent; its determination for our study is provided in the Case Study section. The full pseudocode for the resilience calculation is provided below:

1: Input network G, its daily damage state X_d, $d = 0, 1, 2, \ldots, D$, and OD set N^Z
2: for $d = 0, 1, 2, \ldots, D$
3: if $k^Z < k^{Z*}$ # using CNM
4: Calculate c_{ij}^R for all $i.j \in N^C$ via G^R under X_d using the Dijkstra algorithm, and build network G^{CHA};
5: Calculate $c_{ij}(t)$ via G^{CHA} under X_d using MTTA for all $i.j \in N^Z$ and $t \in DT$;
6: else # using SCM
7: Calculate c_{ij}^R for all $i.j \in N^C$ via G^R under X_d using the Dijkstra algorithm, and build network G^{IHA};

(continued on next page)

(*continued*)

8: Calculate $c_{xy}^{IHA}(t)$ via G^{IHA} under X_d using MTTA for all $x,y \in N^I$ and $t \in DT$;
9: Obtain $c_{ij}(t)$ for all $i,j \in N^Z$ and $t \in DT$ according to Eq. (8);
10: end
11: Get $a_d = \{a_{ij}(d)\}$ according to Eq. (5);
12: Get A_d according to Eq. (4);
11: end
12: Obtain RL based on Eq. (7).

4. Case study

This section analyzes the travel time resilience of the coupled road, HSR, and airline system in mainland China (Fig. 6). According to the 2020 administrative division of China [89], there exist 363 prefecture-level cities in mainland China (Fig. 6a). This section focuses on inter-city travels and each of the 363 prefecture-level cities ($k^Z = 363$) is represented by one OD representative node, taken as the road intersection nearest the city's urban centroid. These cities can be further grouped at eight economic zones level or 31 provinces level. The eight economic zones consist of northeast China (NEC), northern coastal China (NCC), southern coastal China (SCC), eastern coastal China (ECC), middle reaches of the Yellow River (MRYLR), middle reaches of the Yangtze River (MRYTR), southwest China (SWC), and northwest China (NWC) (Fig. 6b).

Data and parameters: The road network in mainland China is available from the Geofabrik's free download server [90], which contains 4258,800 nodes and 5228,683 edges, and the travel speed on each edge is assigned based on the edge type [91]. The railway and airline timetable information in other countries can be sourced from national transport departments or ticketing platforms [58]. There are totally 1284 high-speed stations and 238 airports ($k^I = 1522$). The population movement flow data for 2020–01–01 to 2020–02–25 and 2021–09–13 to 2022–03–10 are obtained from Baidu migration [92], which reports city-pair flows. Specifically, because the daily OD series does not cover the Zhengzhou rainstorm or the Shanghai lockdown windows, this section constructs a time-invariant baseline OD matrix f_d by averaging daily flows over the available periods and holding it fixed across days. The statistical data, including urban population and GDP, are obtained from the statistical yearbook of regions in China [93]. Following the recommendations of most Chinese airports and train stations [94], the time needed to enter a station (or an airport), exit from a station (or an airport), and transfer inside a station (or an airport) is set as 30 min (or 60 min), 15 min (or 30 min), 30 min (or 60 min), respectively [69]. The experiments are performed on a laptop with Intel i5 11300H quad-core @3.10 GHz and 16GB memory.

4.1. Computational cost analysis of the resilience assessment methods

This section tests the computational cost of the CNM and SCM in the resilience assessment of the NMTS in mainland China. Note that the computational cost C^{RL} for the resilience loss RL is approximately equal to the sum of the computational cost C^a for the travel time matrix $\boldsymbol{a}$ - under all time periods ($\kappa = 0, 1, 2, \ldots, K$), i.e., $C^{RL} \approx C^a * (K+1)$. The experiments thus compare the computational cost of the two methods in terms of C^a. Theoretically, the value of C^a depends on the number of representative nodes k^Z in NMTS with fixed k^I and k^R. Fig. 7 shows C^a as a function of k^Z for the two methods, where k^Z representative nodes are randomly selected from road nodes with k^Z from one to 1600. From the figure, the computational cost of the CNM is the quadratic function of k^Z, with $C^a_{CNM} = 0.000019k^{Z2} + 0.0038k^Z + 2.6$; while the computational cost of the SCM is linearly correlated with k^Z, with $C^a_{SCM} = 0.0017k^Z + 68.74$. Also, results show that there exists a critical k^Z, i.e., $k^{Z*} = 1143$. The CNM is more applicable when $k^Z < k^{Z*}$, while the SCM is more time-saving when $k^Z > k^{Z*}$.

In summary, the CNM is more applicable for those scenarios of small k^Z, especially when it is considerably smaller than the number of intermodal access nodes k^I. On the contrary, the SCM is more suitable for those scenarios of large k^Z. Despite that the critical threshold for k^Z (1143 in mainland China) may vary depending on the case system of concern, the proposed two methods offer a comprehensive solution for addressing the travel time-based resilience problem in diverse scenarios. Considering that the case study section defines system functionality based on the travel time among 363 cities ($k^Z = 363$), the CNM is thus the most time-saving method with $C^a_{CNM} = 20.77$ h (Fig. 6), and the subsequent experiments use the CNM to support the resilience estimation and analysis.

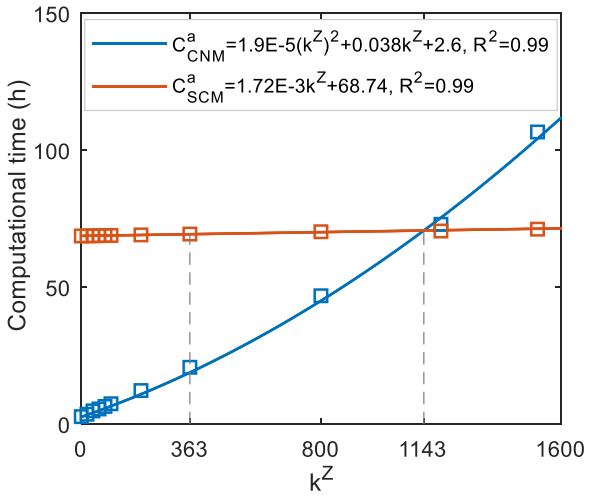

Fig. 7. C^a as a function of k^Z using the two solution methods, respectively. the blue and brown rectangles denote the real values of C^a_{CNM}, C^a_{SCM}, respectively, and the two lines are the corresponding fitting curves.

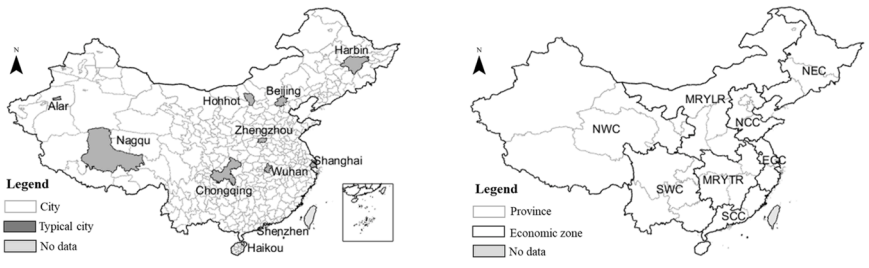

(a) (b)

Fig. 6. The study area and zone division. (a) city-level division of mainland China, cities colored dark grey are typical cities mentioned in the result analysis. (b) province- and economic zone-level divisions of mainland China.

4.2. Resilience assessment of NMTSs under city lockdown

Following COVID-19 outbreaks, China implemented regional lockdowns—notably the metropolitan quarantine of Wuhan (≈76 days) and the dynamic lockdown of Shanghai (≈66 days). In the case study, a lockdown is approximated as a spatially localized, synchronous close–reopen within the locked area for two pragmatic reasons. First, Wuhan's enforcement and reopening were essentially step-like—the government lockdown order instructed residents not to leave the city and suspended all access via airports, railway stations, and freeway entrances at 10:00 on 23 January 2020. Second, component-level daily closure and reopening records for other city lockdowns are rarely available nationally, and a uniform specification aids cross-city comparability. Operationally, this section disables all road edges whose centroids lie in or cross the locked area; suspends all trains or flights whose origins or destinations are inside the locked area; and allows through services to skip in-region stops while operating outside. Links in network G are marked disrupted if any element in their associated component set fails (Eq. (3)), and all affected elements are assumed to fail at lockdown start and resume at lockdown end.

Due to the prolonged duration of city lockdowns, passengers within the locked-down cities could experience travel delays lasting several months, rendering average delay metrics less meaningful for assessing the disruption. Therefore, this section adopts the proportion of affected passengers (PAP) to capture the impact of the lockdown. During Wuhan's lockdown, an average of 3.84 % of NMTS passengers were affected per day—1.35 times higher than the actual passenger flows entering or exiting the city (2.84 %). The overall resilience loss associated with Wuhan's lockdown was 2.92 (Fig. 8a). Geographically, the impact exhibited a clear spatial radiation pattern, with PAP values decreasing outward from Wuhan (Fig. 8b). In particular, four cities within the Wuhan metropolitan area—Xiaogan, Xianning, Huanggang, and Ezhou—experienced PAP values exceeding 60 %, with the affected passengers (excluding direct Wuhan flows) suffering an average travel delay of 61.47 min. Moreover, 18 cities, primarily located in Hubei Province, experienced PAP values above 15 %, with an average travel delay of 28.93 min. These widespread impacts are largely attributable to Wuhan's central role as a regional transport hub. A similar pattern was observed during Shanghai's lockdown, where 6.35 % of NMTS passengers were affected daily—1.53 times the proportion of direct flows to and from Shanghai (4.15 %). Only one city, Suzhou, had a PAP value above 50 %, and the average travel delay there was relatively modest at 17.43 min, reflecting the more robust and redundant transport network surrounding Shanghai (Fig. 8c). However, nearly half cities had over 1 % of passengers affected, underscoring Shanghai's significance as a national transport hub despite the availability of alternative routes.

In addition, the experiments assess the resilience loss under the lockdown of each city, with the lockdown duration set as 76 days for comparison purposes. The resilience loss map depicted in Fig. 9a shows an obvious spatial imbalance, with the daily PAP ranging from 0.01 % to 10.07 %. Guangzhou ($RL = 7.65$), Shenzhen ($RL = 5.40$), Shanghai ($RL = 4.83$) are the top three cities whose lockdowns bring the largest resilience loss; while the lockdown of Nagqu or Chamdo has little impact on inter-city travel, with $RL < 0.02$. At the province level, the highest resilience loss is associated with three municipalities directly under the Central Government of Shanghai, Beijing, and Tianjin ($RL > 1.8$). There are three provinces with the lowest average resilience loss over their comprised cities, i.e., Tibet, Gansu, and Qinghai, with the RL smaller than 0.1. At the economic zone level, the highest average resilience loss is resulted from the lockdown of cities in the ECC with the mean RL as 1.35, followed by the SCC of 0.94, the NCC of 0.91. The NEC and NWC have the smallest average resilience loss with the mean RL as 0.32 and 0.08, respectively (Fig. 9b). The experiments also examined spatial dependence in the RL field. A global Moran's I test indicates significant

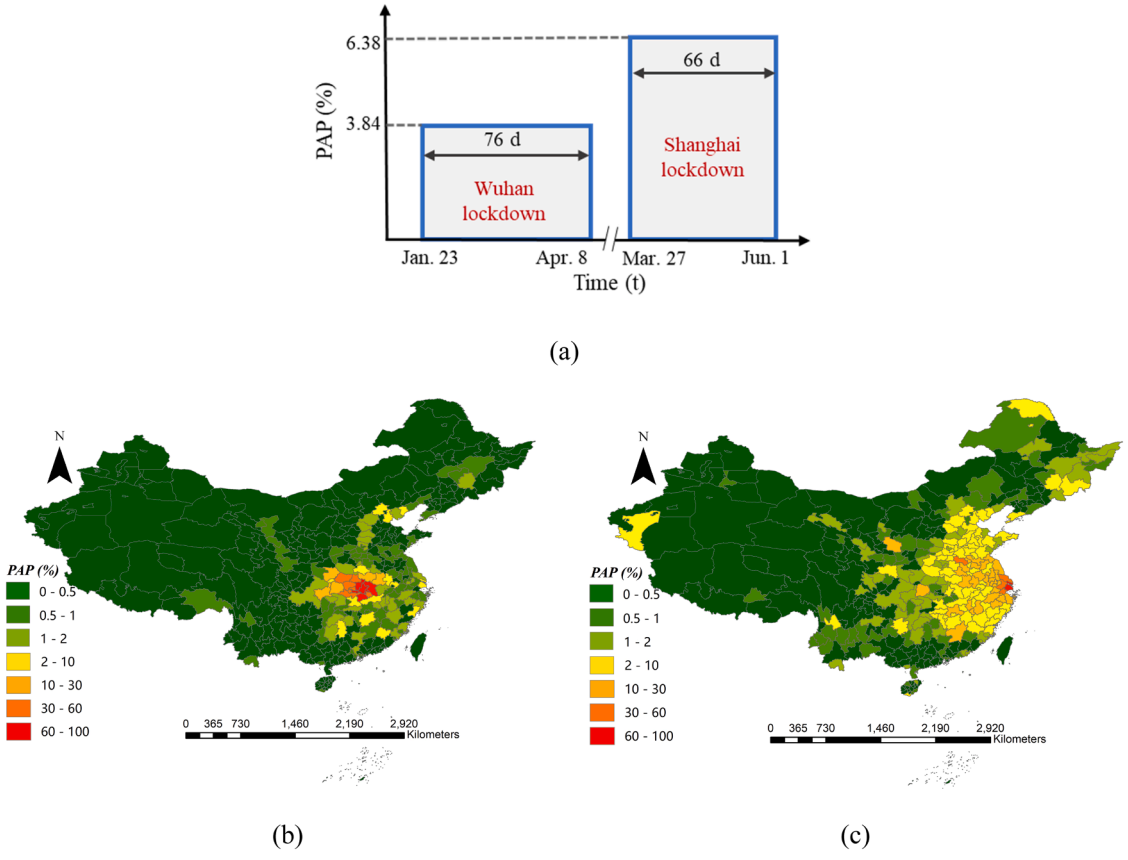

Fig. 8. (a) The PAP changes under the lockdown of Wuhan and Shanghai. The PAP of each city due to the lockdown of (b) Wuhan and (c) Shanghai.

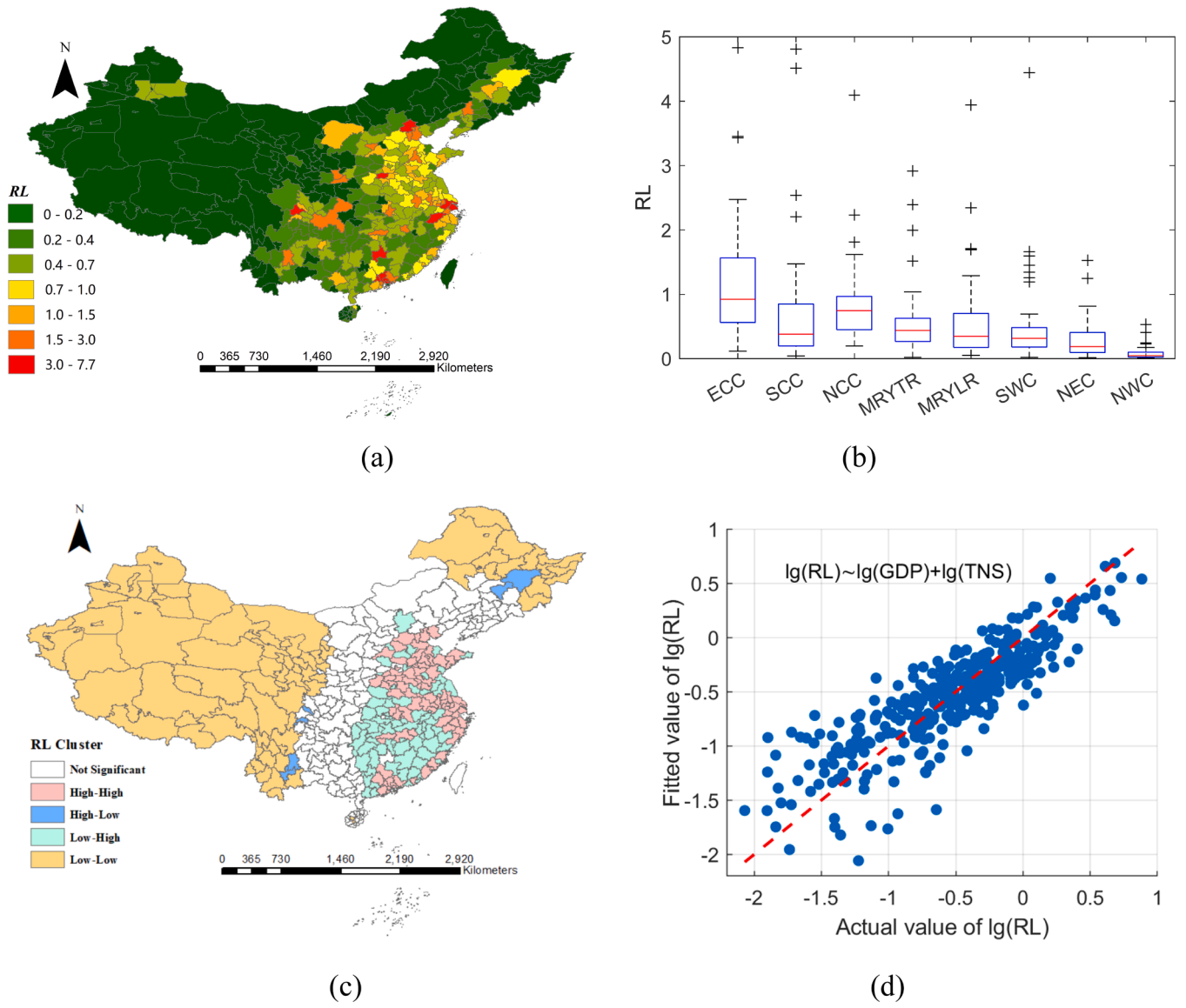

Fig. 9. (a) The resilience loss map under the lockdown of each city. (b) the boxplots of resilience losses for cities in the eight economic zones. (c) LISA cluster map of *RL* at city scale. (d) relationships between $\log_{10}RL$, $\log_{10}GDP$ and $\log_{10}TNS$.

positive autocorrelation ($I = 0.14$, $p < 0.001$), and a local indicators of spatial association (LISA) analysis reveals clear clusters—large LL belts in the west and HH/HL pockets along the east—consistent with regional agglomeration.

To investigate the factors driving the spatial impact patterns, this section employs a city-level linear mixed model considering six indicators: GDP, number of city population (NCP), number of road nodes (NRN), number of high-speed trains that stop inside the city (NHT), number of flights that stop inside the city (NAF), and a transport network size-related indicator, TNS I (sum of normalized NRN, NHT, NAF). The experiments test alternative functional forms (logs, squares, products/interactions) and the best specification is lg (RL) ~lg (GDP) + lg (TNS), with fixed slopes of 0.74 for lg (GDP) and 0.14 for lg (TNS) (Fig. 9). GDP had the strongest effect ($p < 0.01$, Hedge's $g = 2.59$), followed by TNS ($p < 0.01$, Hedge's $g = 0.59$). This suggests that well-developed cities with higher GDP and larger transport systems are associated with more resilience loss due to their lockdowns. Notably, the observed spatial clusters of *RL* closely mirror the spatial dependence of GDP and transport-network size (TNS); accordingly, the city-level model that includes both variables can absorb much of the large-scale spatial structure.

It should also be noted that the real lockdown durations vary among cities. The experiments further produce the lockdown duration of each city using the full-spectrum dynamics model of COVID-19, where the initial conditions and interventions are set the same as Wuhan [95]. Similar spatial disparities in resilience loss and strong correlations between resilience loss and socioeconomic indictors as well as transport network size have also been observed.

4.3. Resilience assessment of NMTSs under rainstorm

This section assesses the resilience loss of NMTSs under the historical rainstorm that occurred on 20, July 2021 in Zhengzhou, Henan province, which has led to the paralysis of road traffic and the temporary closure of several railway stations and airports. Given Zhengzhou's role as a geographical and transportation hub in the disaster-affected region, the rainstorm is modeled as a city-covering disruption centered on Zhengzhou. To model this event, it needs to first identify all transportation components located in the city and set their damage states to failed; all functionality links incident to damaged road intersections or

to station/airport are disabled; any train or flight that stops at or traverses a damaged component is treated as non-operational, and its timetable-related links are failed. Restoration is modeled asynchronously using documented dates—roads on 23 July, air on 24 July, and rail on 29 July—via component-day calendars X_d. The staggered recovery reflects mode-specific safety and operational requirements. Recovery timings differ by mode: roads typically reopen first after drainage, debris removal, and spot inspections; airports follow after runway/taxiway and navigation-aid checks with crew /regulatory readiness; rail lags due to stringent track, power–signal, and corridor-wide safety verifications.

Two indicators are used to quantify the impact of this event: the proportion of affected passengers (PAP) and the average travel delay (ATD). For origin-destination (OD) pairs that were temporarily unreachable, travel time was estimated as the normal travel time plus the number of days until that OD pair became reachable again. The evolution of system functionality over time is shown in Fig. 10a–b. Immediately following the rainstorm, 6.44 % of NMTS passengers were affected, with an average travel delay of 167.12 min. The affected passengers include both direct flows to/from Zhengzhou (3.85 % of NMTS passengers) and transit-dependent through-trips whose MTTA itineraries traverse Zhengzhou (2.59 % of NMTS passengers). During the initial three days (July 20–22), while the road network remained disrupted, the PAP remained constant. While the PAP remained constant over the first three days (July 20–22), the ATD gradually declined to 56.19 min, as inaccessible passengers required fewer days to resume travel. Following road network recovery on July 23, all OD pairs became reachable, leading to a sharp drop in PAP to 3.49 % and a reduction in ATD to 1.19 min. On July 24, the air network was restored, further reducing the PAP to 2.53 % and the ATD to 0.44 min. This level of system performance was sustained until July 29, when rail service was fully restored and normal system functionality was resumed.

The urban-scale spatial distribution of PAP and ATD on July 20 is shown in Fig. 10c–d. A clear spatial pattern emerges: disruptions were most severe in Henan Province, with the highest PAP and ATD values concentrated around Zhengzhou. Four cities—Kaifeng, Xinxiang, Xuchang, and Jiaozuo—recorded PAP values exceeding 60 %, and ATDs greater than 24 h. All cities within Henan experienced PAPs above 20 % and ATDs exceeding 10 h, reflecting their high dependency on Zhengzhou as a regional transport hub. Compared to city lockdown events, the rainstorm produced broader spatial impacts. Cities in remote regions such as Hami, Xinjiang, exhibited non-negligible impacts, with 3.56 % of passengers affected and an ATD of 24.14 min, as many long-distance travel routes from western regions passed through Zhengzhou. This highlights the national-level ripple effects stemming from disruptions in transport hubs. Notably, the spatial distributions of PAP and ATD are strongly correlated, with a Pearson correlation coefficient of 0.94, suggesting that PAP is a reliable proxy for travel delay impacts in

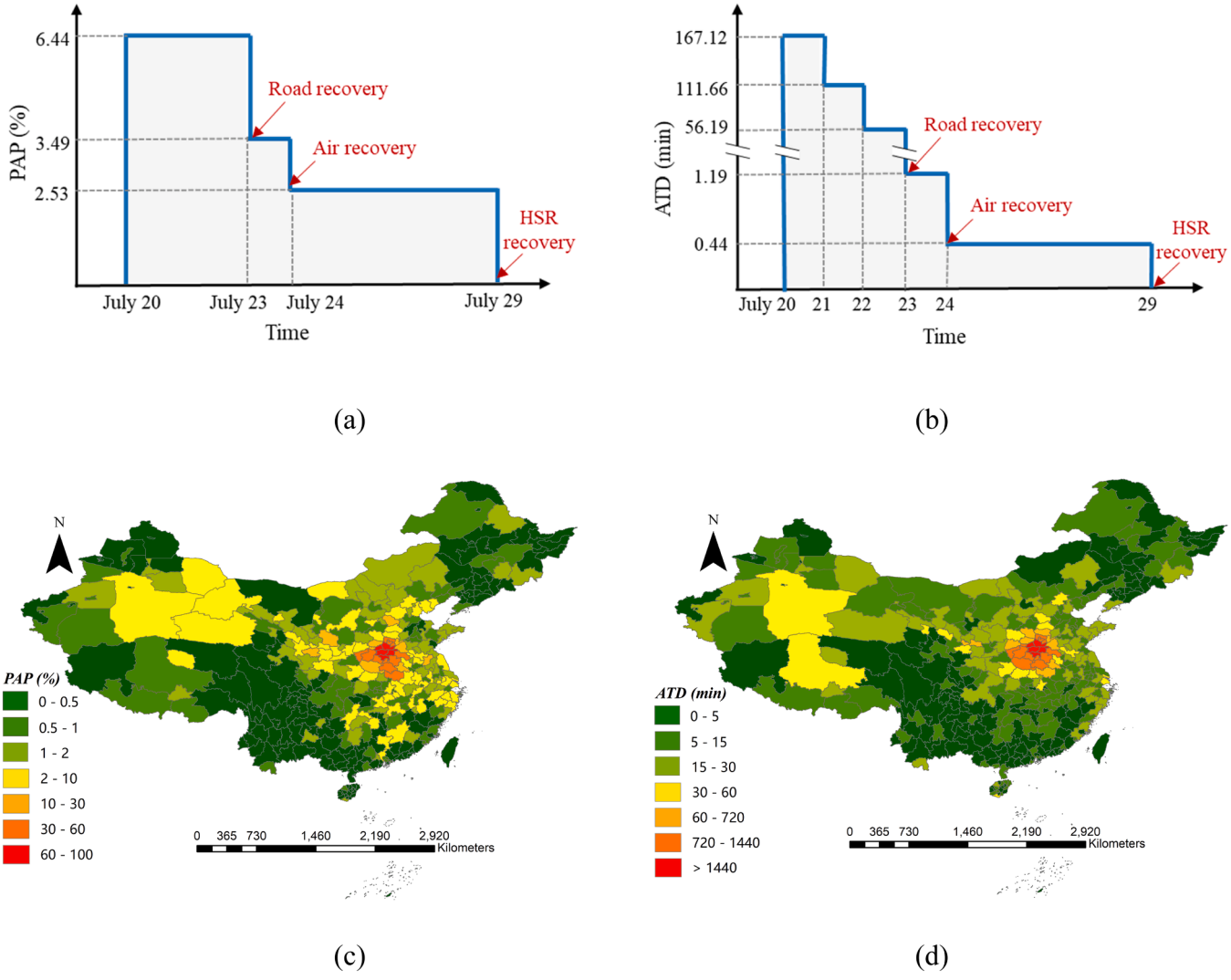

Fig. 10. (a) The PAP and (b) ATD curve under the historical rainstorm in Zhengzhou. the urban scale distribution of (c) PAP and (d) ATD on July 20.

extended disruptions. Similar patterns are observed across other dates, with results presented in the Appendix.

Note that the resilience loss under this event largely depends on when each transport mode returns to full operation. This section next conducts an initial sensitivity analysis, varying the completion day of each transport mode—rail (t_H), road (t_R), and air (t_A)—and evaluating the resulting change in resilience loss (Fig. 11). Ordering the triplet (t_H, t_R, t_A) yields six completion orders (HRA, RHA, HAR, RAH, AHR, ARH); the blue star in Fig. 11 marks the real combination. These orders summarize completion timing only and do not assume strictly serial, uncoordinated repairs—work may proceed in parallel across modes and components. Results show that advancing completion by one day in road, HSR, and air system separately reduces resilience loss by 27.96 %, 21.18 %, and 16.03 %, on average. Thus, expediting road restoration delivers the largest systemwide benefit—reconnecting OD pairs and enabling detours—followed by HSR and then air, underscoring the road network's foundational role in NMTS accessibility and recovery under localized but strategically situated disruptions.

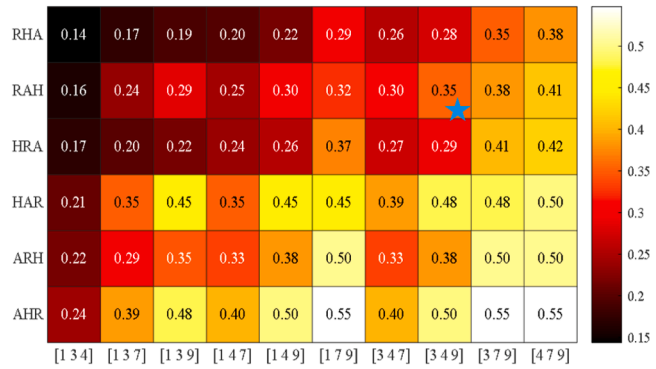

Fig. 11. The resilience loss caused by the city-covering disruption of Zhengzhou under sixty combinations of t_H, t_R, t_A. the y-axis shows six completion orders, with H, R, A representing HSR, road, and airline system, respectively; the x-axis shows ten completion-day triplets (t_1, t_2, t_3). the blue star marks the observed combination.

5. Conclusion and discussion

This study develops a passenger-oriented framework to assess the travel-time resilience of national multimodal transport systems under extreme events. The framework model road, rail, and air in a unified functionality network with explicit timetables and transfers, compute the earliest-arrival itineraries with a proposed Minimum Travel-Time Algorithm (MTTA), and quantify day-by-day functionality and cumulative resilience loss. To address computational challenges posed by large-scale networks, two solution methods are developed: a critical node–based method (CNM) for scenarios requiring OD-specific evaluation, and a segment computation–based method (SCM) for cases with large OD nodes. Applied to mainland China, the framework reveals strong spatial heterogeneity in lockdown impacts: cities with higher GDP and larger transport networks impose greater national-level losses when closed. For the Zhengzhou rainstorm, recovery sequencing matters: prioritizing road restoration consistently minimizes losses, with a one-day acceleration of road, rail, and air recovery reducing resilience loss on average by 27.96 %, 21.18 %, and 16.03 %, respectively. These findings can inspire resilience-based policy-making on national transport systems.

Furthermore, several additional experiments have been conducted to relax some assumptions in this research. The first attempt responds to the travel demand fluctuations under disruptions. Incorporating day-by-day OD demand using Baidu Migration flows for 2020–01–20 to 2020–02–25, the experiment performs a demand-aware resilience analysis for the Wuhan lockdown (Appendix B). The resulting functionality curve exhibits significant disparities compared to the one obtained with fixed travel demand (Fig. 8a and Appendix). This discrepancy is attributed to a notable increase in travel demand during the spring festival and a substantial decrease during the Wuhan lockdown. When daily OD data are available, our proposed framework can directly integrate $\boldsymbol{f}_d$ without any change to the routing or aggregation procedures. Second, to relax the fastest-path assumption and strengthen behavioral realism, the experiment formulates a preference-aware route choice, where itineraries are evaluated by a generalized disutility combining time, fare, transfer penalties, and mode-specific aversion terms (Appendix A.4). Tests in the case system show that realistic preferences can shift both pre- and post-disruption routing and thus alter measured delays. This formulation allows our proposed framework to incorporate traveler preferences and heterogeneity when related data are available. Third, recognizing that travelers do not always select the multi-mode with minimum time, Appendix C reflects mode distributions by allocating each OD's daily demand to road, rail, and air using exogenous baseline shares from the 2024 Statistical Bulletin on the Development of the Transport Industry (Ministry of Transport of China). Under the Wuhan lockdown, the mode-share analysis yields system functionality losses consistent with theory and confirms that the main analysis—based on best multimode (fastest-path) routing—provides a lower bound on travel-time-based impacts.

There are still some limitations in this work. One caveat relates to the approximated modeling of both lockdown and rainstorm as temporally discrete, synchronous, localized close–reopen events, whereas real disruption and recovery under these events often unfold gradually. Where data permit, our framework can directly encode staged, asset-specific disruption and recovery by assigning component–day calendars $x_l(d)$ and can represent partial service $x_l(d) \in \{0, 1\}$ by replacing binary states with a capacity factor $x_l(d) \in [0, 1]$ that propagates into MTTA link times (e.g., reduced speeds). Second, this study models urban roads and intercity expressways as a single layer, without distinguishing their different hazard exposures, damage states, or recovery mechanisms under extreme events, separating these sub-networks is an important direction for future work. It should be also noted, however, that the resilience assessment approach proposed is general and readily extensible to support more complicated application scenarios, such as departure-time- and preference-aware travel-time resilience assessment, critical station and link identification [96,97], transport network expansion planning [51], post-disaster resource-constrained optimization [68], and resilience analysis of more holistic transport systems across regions.

CRediT authorship contribution statement

Hui Zhang: Writing – review & editing, Writing – original draft, Visualization, Methodology, Data curation, Conceptualization. **Min Ouyang:** Writing – review & editing, Funding acquisition, Conceptualization. **Min Xu:** Writing – review & editing, Methodology. **Wenjing Sun:** Data curation. **Liu Hong:** Writing – review & editing. **Duantengchuan Li:** Writing – review & editing, Visualization, Data curation.

Declaration of competing interest

The authors declare no competing interests.

Acknowledgments

This work was supported by the National Key Research and Development Program of China (Grant No. 2023YFC3805100), the National Natural Science Foundation of China (Grant No. 72371109), and the Project of Interdisciplinary Research Support Program in HUST (2023-32).

Appendix A. Worked example: three-city toy NMTS

This appendix illustrates the end-to-end workflow—functionality network modeling, time-dependent travel-time calculation (MTTA), and routing adaptation under disruption—using a stylized system connecting Beijing (BJ), Wuhan (WH), and Shenzhen (SZ) (Appendix Fig. 1a). The physical layers include urban roads and intercity expressways, one rail station per city connected by a single train service (T1), and one airport per city connected by three scheduled flights (F1–F3). Timetables are shown in Appendix Fig. 1b

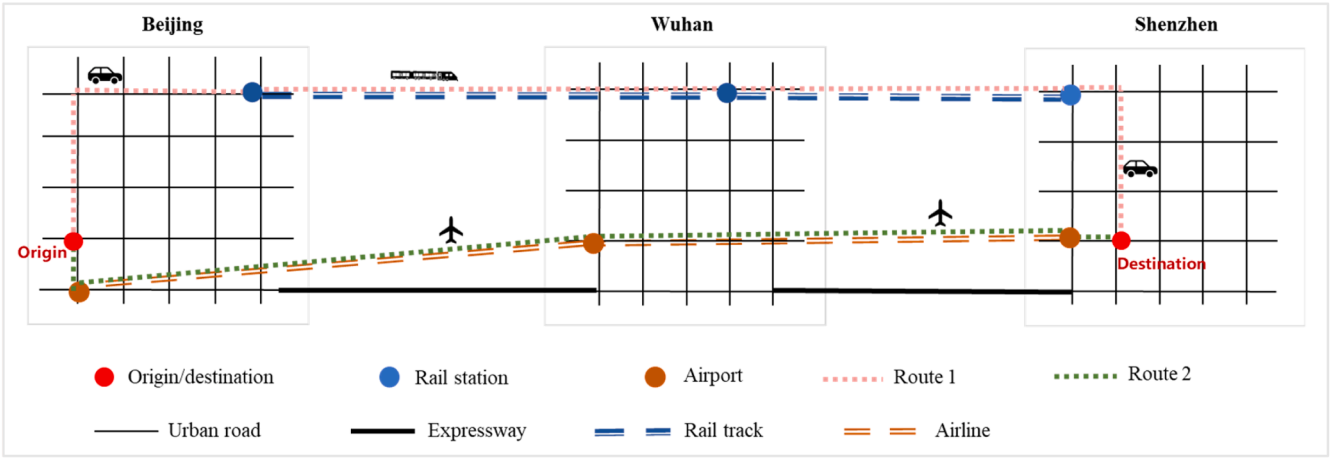

(a)

Train 1					
Stop (city)	code	Arr.	Dep.	Dwell (min)	Fare (CNY)
Beijing	BJR	—	10:00	—	—
Wuhan	WHR	13:55	13:58	3	600
Shenzhen	SZR	18:10	—	—	1000

Flight	Origin (code)	Arr.	Destination (code)	Dep.	Fare (CNY)
F1	Beijing (BJA)	10:00	Wuhan (WHA)	11:50	1000
F2	Wuhan (WHA)	12:00	Shenzhen (SZA)	14:00	800
F3	Beijing (BJA)	14:00	Shenzhen (SZA)	16:00	800

(b)

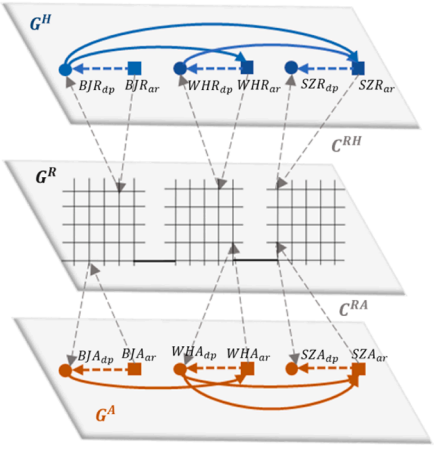

(c)

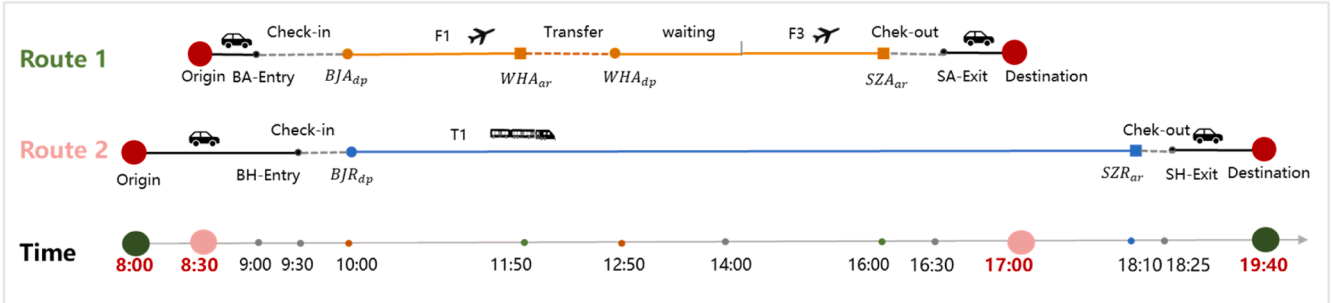

(d)

Appendix Fig. 1. Toy three-city NMTS. (a) physical layers: urban roads and intercity expressways; one rail station and one airport per city. (b) timetables and fares for train T1 and flights F1–F3. (c) A layered functionality network built based on (a) and (b). (d) Itineraries and timeline for Route 1 (green, air via WH) and Route 2 (orange, rail).

A.1. Layered functionality network

We model the network as $G = \{G^R, G^H, G^A, C^{RH}, C^{RA}\}$ with three directed layers—road G^R, rail G^H, air G^A—coupled by intermodal links C^{RH}

(road–rail) and C^{RA} (road–air).

Road layer: Road intersections are nodes; edges represent urban roads (thin black lines) and intercity expressways (thick black lines).

Rail layer: Each station n is represented by a departure node n_{dp} and an arrival node n_{ar}: BJR_{dp}/BJR_{ar} (Beijing rail), WHR_{dp}/WHR_{ar} (Wuhan rail), SZR_{dp}/SZR_{ar} (Shenzhen rail), shown as the blue rectangles and dots in Appendix Fig. 1c. An identical-mode transfer inside each station is modeled by a fixed-time edge $n_{ar}\rightarrow n_{dp}$ (blue dashed lines in Appendix Fig. 1c). The train service T1 generates timetable edges between successive stops, e.g., $BJR_{dp}\rightarrow WHR_{ar}$, $BJR_{dp}\rightarrow SZR_{ar}$ and $WHR_{dp}\rightarrow SZR_{ar}$ (blue solid lines in Appendix Fig. 1c), and these links have departure-time-dependent cost (Eq. (1)).

Air layer: Airports follow the same construction with distinct labels to avoid confusion with rail: BJA_{dp}/BJA_{ar} (Beijing airport), WHA_{dp}/WHA_{ar} (Wuhan airport), SZA_{dp}/SZA_{ar} (Shenzhen airport).

Intermodal access: For each terminal, check-in link from the nearest road node (terminal entrance) to the terminal departure node and check-out link from the terminal arrival node to the nearest road node are added. These links have fixed times reflecting access, screening, and exit. And are represented as the gray dashed line in Appendix Fig. 1c.

A.2. Pre-event routing (Route 1, green — air)

Under normal operation, the fastest itinerary from origin to destination is the two-flight route shown by the green dashed path in the timeline in Appendix Fig. 1d The passenger departs at 08:30, drives on the urban road to Beijing airport entrance (BA-Entry) at 09:00, and, after 30 min of check-in, arrives at BJA_{dp} at 09:30. He waits 30 min for flight F1 and then board Flight F1 (10:00–11:50) and arrive at WHA_{ar} at 11:50. An in-airport transfer brings the passenger to WHA_{dp} at 12:50; since Flight F3 departs at 14:00, the schedule-dependent waiting time on this timetable link is 70 min. The passenger then flies F3 (14:00–16:00) to SZA_{ar} completes check-out to SA-Exit, and takes the final urban road egress to destination, arriving at 17:00. The total generalized travel time for Route 1 is therefore 8 h and 30 min. Under this situation, the weights of the two air timetable edges are:

$BJA_{dp}\rightarrow WHA_{ar}$: 30 min wait + 110 min flight = 140 min;
$WHA_{dp}\rightarrow SZR_{ar}$: 70 min wait + 120 min flight = 190 min.

A.3. Post-event routing (Route 2, orange — rail)

To demonstrate disruption mapping and adaptation, consider a Wuhan weather event that cancels all flights on the study day. The corresponding air timetable links from WHA_{dp} (outbound) and to WHA_{ar} (inbound) are removed from G, and MTTA recomputes the earliest-arrival itineraries on the disrupted network. The resulting fastest option is the rail route (orange line in Appendix Fig. 1a/d). To catch Train T1 (10:00 departure), the passenger leaves at 08:00, reaches the BH-Entry and then BJR_{dp} after access and check-in, rides T1 with the Wuhan in-station dwell, and arrives SZR_{ar} at 18:10. After check-out (to SH-Exit) and the final road leg, the passenger arrives at 19:40. The disrupted-day generalized time is 11 h 40 min, yielding a delay relative to the pre-event itinerary of

$$\Delta a_{ij} = 11\ h\ 40\ min - 8\ h\ 30\ min = 3\ h\ 10\ min$$

This OD-level delay contributes to the daily OD matrix $\boldsymbol{a}_d = \{a_{ij}\}$, the passenger functionality $A_d = F(\boldsymbol{f}_d, \boldsymbol{a}_d)$, and the resilience metrics in Section 3.4.

A.4. Beyond "fastest time": departure-time dependence and preference heterogeneity

In practice, not all travelers depart at a single clock time or choose the minimum-time itinerary. Some may prefer lower monetary cost, fewer transfers, or avoiding air mode (e.g., airsickness). To capture such heterogeneity, we evaluate itineraries using a generalized disutility (cost) that combines time, money, transfers, and optional mode-specific penalties. Let $\mathscr{K}_{ij}(t)$ be the feasible itineraries from i to j when departing at clock time t. For itinerary $\kappa \in \mathscr{K}_{ij}$, define the generalized cost:

$$c_{ij\kappa}(t;\ \boldsymbol{\theta}) = \mathrm{T}_{ij\kappa}(t) + \lambda \mathrm{Fare}_{ij\kappa}(t) + \phi \mathrm{Transfer}_{ij\kappa} + \psi_{air} 1\{air\} + \psi_{rail} 1\{rail\} + \psi_{road} 1\{road\}$$

where $\mathrm{T}_{ij\kappa}(t)$ is the time component produced by MTTA (minutes), including in-vehicle + waiting + transfer time; $\mathrm{Fare}_{ij\kappa}(t)$ is the money cost in this trip; $\mathrm{Transfer}_{ij\kappa}$ is the number of transfers in this trip. The preference vector is $\boldsymbol{\theta} = \{\lambda,\ \phi,\ \psi_{air},\ \psi_{rail},\ \psi_{road}\}$, where λ converts money to minutes via value of time VOT (e.g., VOT = 500 CNY/h, and λ = 0.12 min/CNY), ϕ is a transfer penalty (min per transfer), and ψ_m denotes mode-preference penalties (min) of mode m, allowing, e.g., a disutility for flying. The indicator $1\{\cdot\}$ equals 1 if the itinerary κ uses that mode and 0 otherwise.

(1). Per-departure optimum with heterogeneous preferences. Preferences may vary across travelers; we allow $\boldsymbol{\theta} \sim P(\boldsymbol{\theta})$. The preference-aware OD cost at time t is:

$$a_{ij}(t) = \mathbb{E}_{\boldsymbol{\theta}}\left[\min_{\kappa \in \mathscr{K}_{ij}(t)} c_{ij\kappa}(t;\ \boldsymbol{\theta})\right]$$

For example, setting $\boldsymbol{\theta} = \{0.12,\ 0,0,0,0\}$ retains Route 1 as optimal at $t = 08:30$pre-event. Increasing ϕ (transfer-averse) or setting $\psi_{air} > 0$ (air-averse) may flip the choice to a rail-dominated route (Route 2). This formulation allows the framework to incorporate traveler preferences transparently.

(2). Departure time dependency. OD travel time varies with the departure clock time because timetable-induced waiting and transfers change the door-to-door time. For each departure time t, we calculate the minimum travel cost $a_{ij}(t)$ under time-only preferences ($\boldsymbol{\theta} = 0$), as shown in the figure below. Early and late windows are dominated by air travel, while a mid-morning service gap makes road the fastest option (22 h, flat segment). The vertical dashed line marks $t^* = 08:30$, the best-time departure that attains the minimum travel time (8 h and 30 min; Route 1) over the day Appendix Fig. 2.

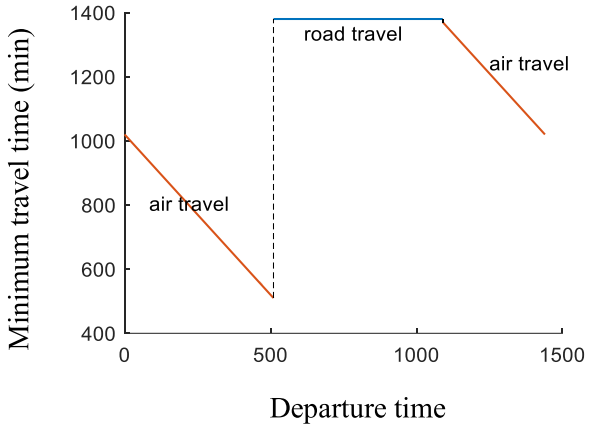

Appendix Fig. 2 Minimum travel time and selected mode versus departure time under normal operation.

(3). Main-analysis assumption. Given the difficulty of obtaining time-resolved OD flows and empirically calibrating $\boldsymbol{\theta}$ at the national scale, the main analysis reports the time-only capability lower bound by setting $\boldsymbol{\theta} = 0$ and allowing travelers to choose the best departure time within the day:

$$a_{ij}(d) = \min_{t \in DT} \min_{\kappa \in \mathscr{K}_{ij}(t)} c_{ij\kappa}(t, \boldsymbol{\theta} = 0)$$

Appendix B. Test incorporating post-disruption travel-flow changes

To reflect both supply (network capability) and demand shifts during extreme events, this experiment evaluates a demand-aware functionality metric based on the number of passengers who can complete their trips within a time threshold τ:

$$A_d = \sum_{i,j \in N^Z} f_{ij}(d) 1\{a_{ij}(d) \le \tau\}$$

where $f_{ij}(d)$ is the observed intercity demand on day d and $a_{ij}(d)$ is the OD generalized travel time computed on the disrupted network $G(X_d)$ via MTTA (Sections 3.3).

Due to data availability, intercity flow data were obtained only for 2020–01–20 to 2020–02–25, spanning the period before and during the Wuhan lockdown. We set τ as 4 h, a commonly used threshold for business travel. The functionality trajectory A_d shows a sharp decline at the onset of restrictions, reaches a trough shortly thereafter, and then partially recovers as limited services and demand resume (Appendix Fig. 3). This curve captures both supply-side loss (service suspensions, closures) and demand-side contraction (fewer attempted trips). This dual sensitivity is valuable for emergency management, where both mechanisms co-determine realized mobility. Appendix Fig. 4, Appendix Fig. 5. The functionality curve of the NMTS in mainland China under the lockdown of Wuhan (2020.1.10–2020.2.25).

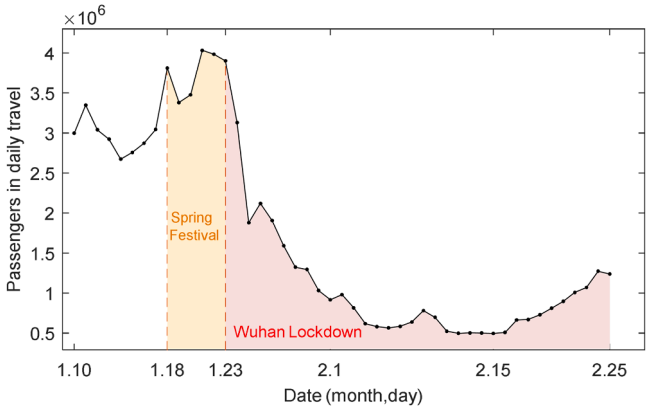

Appendix Fig. 3. The functionality curve of the NMTS in mainland China under the lockdown of Wuhan (2020.1.10–2020.2.25).

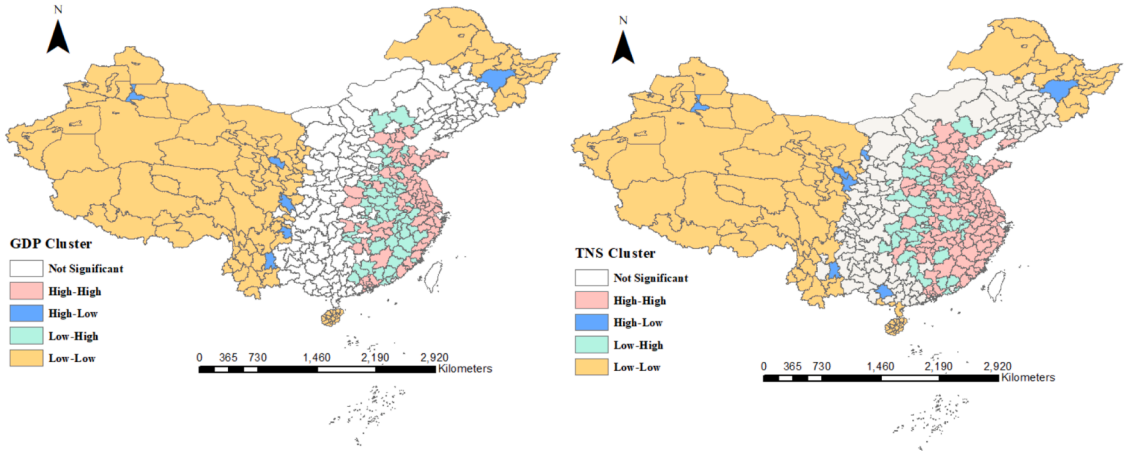

(a) (b)

Appendix Fig. 4. LISA cluster map of (a) GDP and (b) TNS.

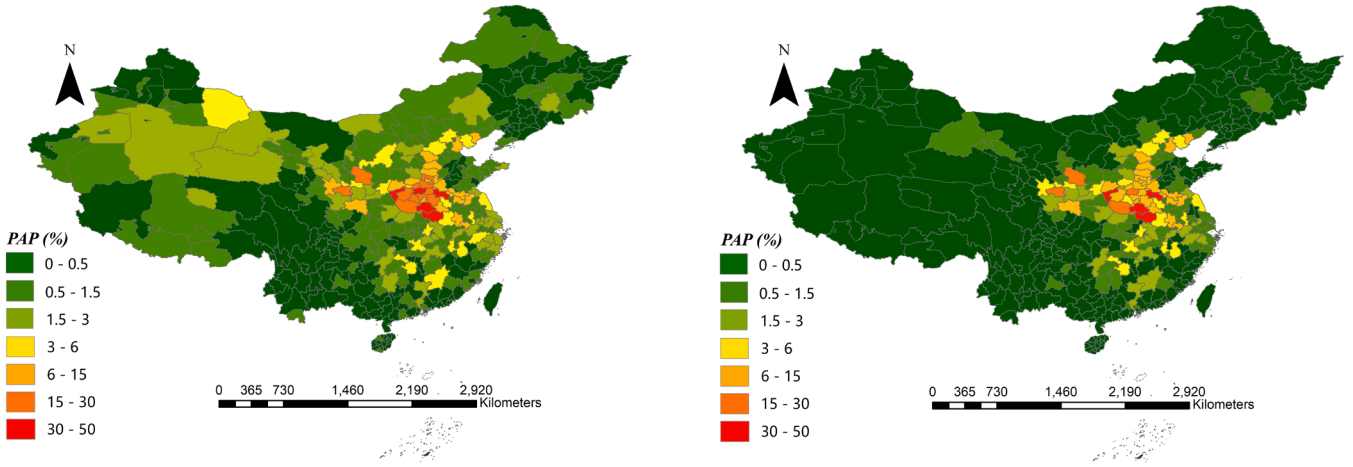

(a) (b)

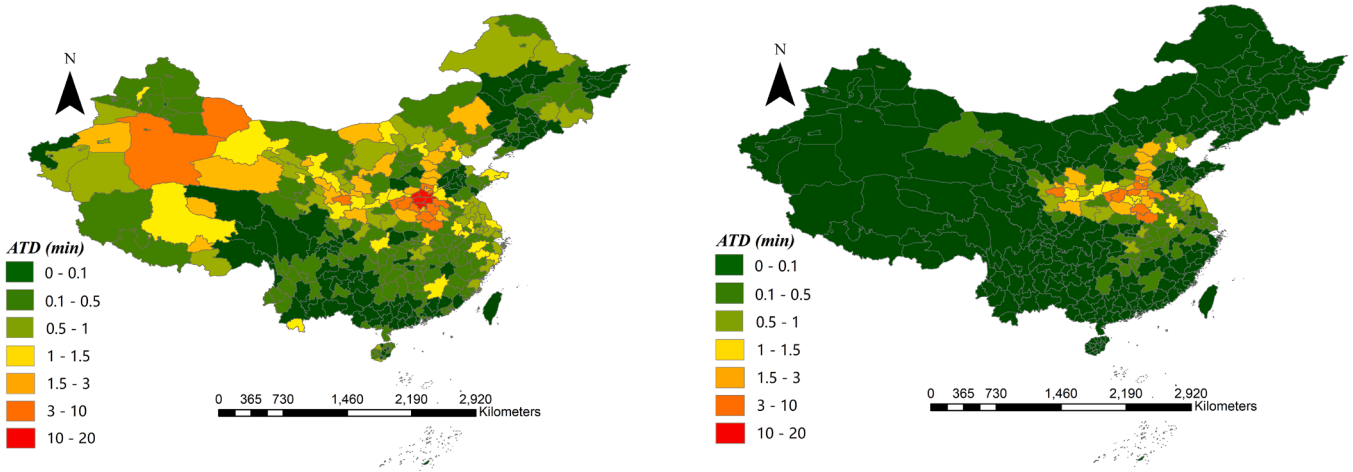

(c) (d)

Appendix Fig. 5. The urban scale distribution of PAP in (a) July 23 and (b) July 24, and ATD in (c) July 23 and (d) July 24.

Appendix C. Test incorporating mode distribution

To reflect the distribution of passengers across travel modes, we allocate each OD's daily demand to road, rail, and air using exogenous baseline mode shares reported in the 2024 Statistical Bulletin on the Development of the Transport Industry (Ministry of Transport of China). The cross-regional mobility composition is: road 91.8 %, rail 6.7 %, air 1.1 %, and water 0.4 %. Because our network models road/rail/air only, we exclude water and renormalize the three modeled modes to sum to 100 %, which produce $s_{road} = 92.17$ %, $s_{rail} = 6.73$ %, $s_{air} = 1.1$ %. For each mode $m \in \{\text{road}, \text{rail}, \text{air}\}$, we compute mode-restricted OD travel times—i.e., itineraries constrained to use only mode m—under both normal operation and disruption, and then evaluate the corresponding mode-wise functionality $\text{PAP}_m(d)$.

Using the Wuhan lockdown as a case, Appendix Fig. 6 plots $\text{PAP}_m(d)$ over time. The lockdown disproportionately affected road ($\text{PAP}_{road} = 4.68$ %) and rail ($\text{PAP}_{rail} = 4.61$ %), whereas air experienced comparatively smaller impacts ($\text{PAP}_{air} = 3.42$ %). We also report a share-weighted functionality curve obtained by re-combining the mode-wise PAPs with the renormalized shares $\text{PAP}^{\text{share}}(d) = \sum s_m \text{PAP}_m(d)$.

As expected, the share-weighted curve $\text{PAP}^{\text{share}}$ lies above the main-analysis PAP^{NMTS} computed under the best multi-mode (fastest-path) assumption, confirming that the main analysis provides a lower bound on travel-time–based impacts.

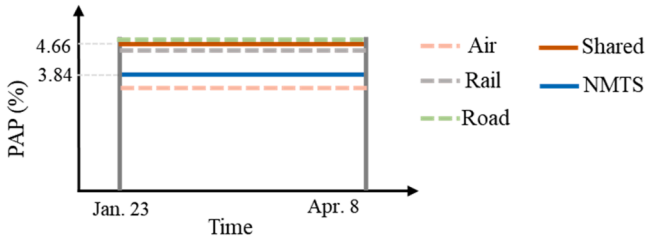

Appendix Fig. 6. The mode-specific functionality curve of the NMTS under the lockdown of Wuhan.

Data availability

Data will be made available on request.

References

[1] Amekudzi-Kennedy A, Singh P, Williams E, Cuadra M, Ashuri B, Woodall B, Dheeraj A. Developing transportation resilience adaptively to climate change. Transp Res Rec 2024;2678(4):835–48.
[2] Avenali A, D'Alfonso T, Reverberi P. Airline-High speed rail cooperation, hub congestion, and airport conduct. Transp Res Logist Transp Rev 2025;194:103818.
[3] Wang K, Jiang C, Ng AKY, Zhu Z. Air and rail connectivity patterns of major city clusters in China. Transp Res Policy Pract 2020:139.
[4] Zhang H, Xu M, Ouyang M. A multi-perspective functionality loss assessment of coupled railway and airline systems under extreme events. Reliab Eng Syst Saf 2024;243:109831.
[5] Zhang H, Zhu Y, Du C, Hong L, Ouyang M, Xu M. Advancing facility accessibility analysis across hierarchies and scales in mainland China. Appl Geogr 2025;179:103611.
[6] Lee E, Kawakita T, Huai Y, Lo HK, Zhang A. Airline and high-speed rail collaboration and competition under travel time variability. Transp Res Policy Pract 2024;185:104104.
[7] Xu G, Gong Y, Zhong L, Zhu D, Liu X, Deng L. To purchase or to sell: capacity agreement in high-speed railway and airline cooperation. Transp Policy 2025;162:84–105.
[8] Ministry of Transport of China, 2024. Statistical bulletin on the development of the transport industry in 2020.
[9] Boura G, Ferguson NS. Incorporating geographic interdependencies into the resilience assessment of multimodal public transport networks. J Transp Geogr 2024;118:103934.
[10] Li S, Zhou Y, Zhang F. Interdependency in transportation system resilience: review and discussion. Transp Res D Transp Environ 2025:104618.
[11] Australian Transport Council. National guidelines for transport system management in australia: 2. strategic transport planning and development. Evaluation; 2006.
[12] Banerjee A, Duflo E, Qian N. On the road: access to transportation infrastructure and economic growth in china (No. w17897). National Bureau of Economic Research; 2012.
[13] Argyroudis SA, Mitoulis SA, Winter MG, Kaynia AM. Fragility of transport assets exposed to multiple hazards: state-of-the-art review toward infrastructural resilience. Reliab Eng Syst Saf 2019;191:106567.
[14] Koks EE, Rozenberg J, Zorn C, Tariverdi M, Vousdoukas M, Fraser SA, Hallegatte S. A global multi-hazard risk analysis of road and railway infrastructure assets. Nat Commun 2019;10(1):2677.
[15] Marchesini I, Althuwaynee O, Santangelo M, Alvioli M, Cardinali M, Mergili M, Rossi M. National-scale assessment of railways exposure to rapid flow-like landslides. Eng Geol 2024;332:107474.
[16] Zhao J, Liu K, Wang M. Exposure analysis of Chinese railways to multihazards based on datasets from 2000 to 2016. Geomat Nat Hazards Risk 2020;11(1):272–87.
[17] Fan C, Jiang X, Lee R, Mostafavi A. Equality of access and resilience in urban population-facility networks. NPJ Urban Sustain 2022;2(1):9.
[18] Ma W, Lin S, Ci Y, Li R. Resilience evaluation and improvement of post-disaster multimodal transportation networks. Transp Res Policy Pract 2024;189:104243.
[19] Ma Z, Yang X, Chen A, Zhu T, Wu J. Assessing the resilience of multi-modal transportation networks with the integration of urban air mobility. Transp Res Policy Pract 2025;195:104465.
[20] Liu T, Fan C. Impacts of disaster exposure on climate adaptation injustice across us cities, 89. Sustainable Cities and Society; 2023, 104371.
[21] Ricciardi G, Ellena M, Barbato G, Alcaras E, Parente C, Carcasi G, Mercogliano P. Risk assessment of national railway infrastructure due to sea-level rise: an application of a methodological framework in Italian coastal railways. Environ Monit Assess 2024;196(9):822.
[22] The State Council of China. 2020. Outline for building a strong transportation country.
[23] Bergantino AS, Gardelli A, Rotaris L. Assessing transport network resilience: empirical insights from real-world data studies. Transp Rev 2024;44(4):834–57.
[24] Knoester MJ, Bešinović N, Afghari AP, Goverde RM, van Egmond J. A data-driven approach for quantifying the resilience of railway networks. Transp Res Policy Pract 2024;179:103913.
[25] Wandelt S, Zhang A, Sun X. Global Airport Resilience Index: towards a comprehensive understanding of air transportation resilience. Transp Res D: Transp Environ 2025;138:104522.
[26] Sun J, Chow AC, Madanat SM. Multimodal transportation system protection against sea level rise. Transp Res D Transp Environ 2020;88:102568.
[27] Wang Y, Zhao O, Zhang L. Modeling urban rail transit system resilience under natural disasters: a two-layer network framework based on link flow. Reliab Eng Syst Saf 2024;241:109619.
[28] Wang Z, Pei Y, Zhang J, Gao Z. Dynamic vulnerability analysis of multi-modal public transport network using generalized travel costs from a multi-layer perspective. Reliab Eng Syst Saf 2025:111375.
[29] Hao H, Yao E, Chen R, Pan L, Wang Y. Dynamic Passenger Route Guidance in the Multimodal Transit System With Graph Representation and Attention Based Deep Reinforcement Learning. IEEE Trans Intell Transp Syst 2024.
[30] Yao Z, Nie L, Fu H. Railway line planning with passenger routing: direct-service network representations and a two-phase solution approach. Transp Res B: Methodol 2024;186:102989.
[31] Zhang H, Zhan B, Ouyang M. Enhancing accessibility through rail transit in congested urban areas: a cross-regional analysis. J Transp Geogr 2024;115:103791.
[32] Asadabadi A, Miller-Hooks E. Assessing strategies for protecting transportation infrastructure from an uncertain climate future. Transp Res Policy Pract 2017;105:27–41.
[33] Shang WL, Ochieng W, Chen Y, Xie C. Resilience of transportation systems under uncertainty. Transp Res Policy Pract 2025:191(C).
[34] Faturechi R, Miller-Hooks E. Travel time resilience of roadway networks under disaster. Transp Res B Methodol 2014;70:47–64.

[35] Kasmalkar IG, Serafin KA, Miao Y, et al. When floods hit the road: resilience to flood-related traffic disruption in the San Francisco Bay Area and beyond. Sci Adv 2020;6(32):eaba2423.
[36] Faturechi R, Miller-Hooks E. Measuring the performance of transportation infrastructure systems in disasters: a comprehensive review. J Infrastruct Syst 2015;21(1):04014025.
[37] Xiao Y, Li Y, Liu W, Wang Z, Chen J, Wang W. Resilience assessment of High-speed railway networks from the spatio-temporal perspective: a case study in Jiangsu Province, China. Reliab Eng Syst Saf 2025;259:110900.
[38] Arnette AN, Zobel CW. A risk-based approach to improving disaster relief asset pre-positioning. Prod Oper Manag 2019;28(2):457–78.
[39] Mao D, Wang P, Fang YP, Ni L. Understanding district heating networks vulnerability: a comprehensive analytical approach with controllability consideration. Sustain Cities Soc 2024;101:105068.
[40] Chen A, Kasikitwiwat P. Modeling capacity flexibility of transportation networks. Transp Res Policy Pract 2011;45(2):105–17.
[41] Li X, Huang W. Resilience quantification method of high-speed railway train diagram under operation section interference: strategies and practices. Reliab Eng Syst Saf 2025;260:111020.
[42] Arango E, Nogal M, Yang M, Sousa HS, Matos JC, Stewart MG. Resilience assessment in post-wildfire recovery of road transport networks by dynamic thresholds and characteristic curves. Reliab Eng Syst Saf 2025:111365.
[43] Chen L, Miller-Hooks E. Resilience: an indicator of recovery capability in intermodal freight transport. Transp Sci 2012;46(1):109–23.
[44] Hosseini S, Barker K, Ramirez-Marquez JE. A review of definitions and measures of system resilience. Reliab Eng Syst Saf 2016;145:47–61.
[45] Chen Z, Zhu S, Feng H, Zhang H, Li D. Coupling dynamics of urban flood resilience in china from 2012 to 2022: a network-based approach, 118. Sustainable Cities and Society; 2025, 105996.
[46] Li T, Rong L, Yan K. Vulnerability analysis and critical area identification of public transport system: a case of high-speed rail and air transport coupling system in China. Transp Res Policy Pract 2019;127:55–70.
[47] Yin L, Zhu J, Li W, Wang J. Vulnerability Analysis of Geographical Railway Network under Geological Hazard in China. ISPRS Int J Geo Inf 2022;11(6):342.
[48] Yoo S, van Wee B, Molin E. Long distance accessibility by air transportation: a literature review. Transp Rev 2024;44(4):811–33.
[49] Duan J, Zeng G, Serok N, Li D, Lieberthal EB, Huang HJ, Havlin S. Spatiotemporal dynamics of traffic bottlenecks yields an early signal of heavy congestions. Nat Commun 2023;14(1):8002.
[50] Wang W, Yang S, Stanley HE, et al. Local floods induce large-scale abrupt failures of road networks. Nat commun 2019;10(1):1–11.
[51] Fan D, Sun B, Dui H, Zhong J, Wang Z, Ren Y, Wang Z. A modified connectivity link addition strategy to improve the resilience of multiplex networks against attacks. Reliab Eng Syst Saf 2022;221:108294.
[52] Chen Z, Wang Y. Impacts of severe weather events on high-speed rail and aviation delays. Transp Res D Transp Environ 2019;69:168–83.
[53] Fang C, Chu Y, Fu H, et al. On the resilience assessment of complementary transportation networks under natural hazards. Transp Res D Transp Environ 2022;109:103331.
[54] Hong L, Ye B, Yan H, et al. Spatiotemporal vulnerability analysis of railway systems with heterogeneous train flows. Transp Res Policy Pract 2019;130:725–44.
[55] Zhu W, Liu K, Wang M, Ward PJ, Koks EE. System vulnerability to flood events and risk assessment of railway systems based on national and river basin scales in China. Nat Hazards Earth Syst Sci 2022;22(5):1519–40.
[56] Li T, Rong L. Spatiotemporally complementary effect of high-speed rail network on robustness of aviation network. Transp Res Policy Pract 2022;155:95–114.
[57] Janić M. Modeling the resilience of an airline cargo transport network affected by a large scale disruptive event. Transp Res D Transp Environ 2019;77:425–48.
[58] Woodburn A. Rail network resilience and operational responsiveness during unplanned disruption: a rail freight case study. J Transp Geogr 2019;77:59–69.
[59] Chen J, Liang C, Liu J, Du B, Yin Y, Peng Q. Resilience assessment of a highway–railway complementary network under rainstorms. Transp Res D Transp Environ 2023;121:103841.
[60] Deng J, Zhai H, Wang Z. Vulnerability evaluation of high-speed railway network under wind disasters. Reliab Eng Syst Saf 2025:111323.
[61] Fang C, Wang M, Fu H, Chu Y, Zio E. A framework for resilience assessment of transportation networks exposed to geohazard threats. Risk Anal 2025;45(8):2255–66.
[62] Kamalian L, Li H, Poo MCP, Bras AA, Ng AK, Yang Z. Analysis of the impact of climate-driven extreme weather events (EWEs) on the UK train delays: a data-driven BN approach. Reliab Eng Syst Saf 2025:111189.
[63] Voltes-Dorta A, Rodríguez-Déniz H, Suau-Sanchez P. Vulnerability of the European air transport network to major airport closures from the perspective of passenger delays: ranking the most critical airports. Transp Res Policy Pract 2017;96:119–45.
[64] Xue F, Zeng Y, Liang J, Ma X, Luo Y. Disturbance impact of rainfall on train travel time in China's high-speed railway network under different spatial–temporal scenarios. Transp Res Logist Transp Rev 2025;198:104102.
[65] Zhang H, Ge Y, Lin J, Xu M, Ouyang M. Amplified impacts of tropical cyclone-induced compound wind-rain hazards on high-speed rail passengers. Transp Res D Transp Environ 2025;148:105023.
[66] Jiao J, Zhang F, Liu J. A spatiotemporal analysis of the robustness of high-speed rail network in China. Transp Res D Transp Environ 2019;89:102584.
[67] Wang Y, Cao X, Qin F, Tong L. Vulnerability analysis of the Chinese coupled aviation and high-speed railway network. Chin J Aeronaut 2022;35(12):189–99.
[68] Szymula C, Bešinović N. Passenger-centered vulnerability assessment of railway networks. Transp Res B Methodol 2020;136:30–61.
[69] Hong L, Ouyang M, Xu M, et al. Time-varied accessibility and vulnerability analysis of integrated metro and high-speed rail systems. Reliab Eng Syst Saf 2020;193:106622.
[70] Zhang H, Ouyang M, Sun W, Hong L. An approach for accessibility assessment and vulnerability analysis of national multimodal transport systems. Risk Anal 2023;43(11):2312–29.
[71] Tang Y, Li S, Zhai C, Zhao J. Railway operation recovery method of regional high-speed railway based on optimal resilience after earthquakes. Reliab Eng Syst Saf 2023;238:109400.
[72] Li S, Tang Y, Zhai C. Earthquake resilience assessment and improving method of high-speed railway based on train timetable rescheduling. Int J Disaster Risk Reduct 2022;82:103361.
[73] Zhang T, Niu C, Nair DJ, Dixit V, Waller ST. Equity analysis and improvement in transportation resilience optimisation at the pre-event stage. Transp Res D Transp Environ 2023;122:103892.
[74] Feng X, He S, Chen X, et al. Mitigating the vulnerability of an air-high-speed railway transportation network: from the perspective of predisruption response. Proc Inst Mech Eng J Risk Reliab 2021;235(3):474–90.
[75] Jing Y, Yang X, Yang Y, Jiao J, Yuan Y, Lu C, Dui H. Reliability evaluation and multi-stage performance analysis of multi-state air-ground cooperative networks for city aviation and railway infrastructure. Reliab Eng Syst Saf 2025:111500.
[76] Misra S, Padgett JE. Estimating extreme event resilience of rail–truck intermodal freight networks: methods, models, and case study application. J Infrastruct Syst 2022;28(2):04022013.
[77] Chen M, Lu H. Analysis of transportation network vulnerability and resilience within an urban agglomeration: case study of the greater Bay area China. Sustainability 2020;12(18):7410.
[78] Stamos I, Mitsakis E, Salanova JM, et al. Impact assessment of extreme weather events on transport networks: a data-driven approach. Transp Res D Transp Environ 2015;34:168–78.
[79] Geurs KT, Van Wee B. Accessibility evaluation of land-use and transport strategies: review and research directions. J Transp geogr 2004;12(2):127–40.
[80] Handy SL, Niemeier DA. Measuring accessibility: an exploration of issues and alternatives. Environ Plan A 1997;29(7):1175–94.
[81] Hansen WG. How accessibility shapes land use. J Am Inst plan 1959;25(2):73–6.
[82] Stokes EC, Seto KC. Tradeoffs in environmental and equity gains from job accessibility. Proc Natl Acad Sci 2018;115(42):E9773–81.
[83] Weiss DJ, Nelson A, Gibson HS, et al. A global map of travel time to cities to assess inequalities in accessibility in 2015. Nature 2018;553(7688):333–6.
[84] Zhang T, Niu C, Nair DJ, Robson EN, Dixit V. Transportation resilience optimization from an economic perspective at the pre-event stage. Sustain Anal Model 2023;3:100027.
[85] Dijkstra EW. A note on two problems in connexion with graphs. Numerische Mathematik 1959;1(1):269–71.
[86] Bruneau M, Chang SE, Eguchi RT, et al. A framework to quantitatively assess and enhance the seismic resilience of communities. Earthq Spectra 2003;19(4):733–52.
[87] Christodoulou A, Dijkstra L, Christidis P, et al. A fine resolution dataset of accessibility under different traffic conditions in European cities. Sci Data 2020;7(1):1–10.
[88] Wu H, Levinson D, Sarkar S. How transit scaling shapes cities. Nat Sustain 2019;2(12):1142–8.
[89] Ministry of Civil Affairs of China. 2021. www.mca.gov.cn/article/sj/xzqh/2020/20201201.html.
[90] Geofabrik, 2020. Download OpenStreetMap data for this region: asia. https://download.geofabrik.de/asia.html.
[91] Weiss DJ, Nelson A, Vargas-Ruiz CA, et al. Global maps of travel time to healthcare facilities. Nat Med 2020;26(12):1835–8.
[92] Baidu Migration, 2022. https://qianxi.baidu.com/#/.
[93] National Bureau of Statistics of China. 2021. China Regional Statistical Yearbook.
[94] Zhu Z, Zhang A, Zhang Y. Measuring multi-modal connections and connectivity radiations of transport infrastructure in China. Transp Transp Sci 2019;15(2):1762–90.
[95] Hao X, Cheng S, Wu D, et al. Reconstruction of the full transmission dynamics of COVID-19 in Wuhan. Nature 2020;584(7821):420–4.
[96] Bagloee SA, Sarvi M, Wolshon B, Dixit V. Identifying critical disruption scenarios and a global robustness index tailored to real life road networks. Transp Res Logist Transp Rev 2017;98:60–81.
[97] Niu C, Jian S, Nair D, Dixit V. Pre-disaster resilient road network investment strategy with uncertainty quantification. IEEE Trans Intell Transp Syst 2023;24(7):6849–64.